Towards Quantum Limited Detectors for the MADMAX Axion Dark Matter Search: Investigation of Dielectric Losses in Josephson Parametric Amplifiers

Master thesis at the Faculty of Physics
of
Ludwig-Maximilians-University Munich

submitted by
Georg Monninger
born in Heidelberg

Munich, 15 March 2023

Auf dem Weg zu quantenbegrenzten Detektoren für die Suche nach dunkler Materie Axionen bei MADMAX: Untersuchung dielektrischer Verluste in parametrischen Josephson-Verstärkern

Masterarbeit der Fakultät für Physik
der
Ludwig-Maximilians-Universität München

vorgelegt von
Georg Monninger
geboren in Heidelberg

München, den 15.03.2023

Abstract

MADMAX is an experiment for the search of dark matter axions. In order to achieve the required sensitivity for detection, preamplifiers are needed that operate at or close to the quantum limit. Traveling wave parametric amplifiers (TWPA) are a promising tool for accomplishing this in the frequency range around 20 GHz. To reach standard quantum limit, an open challenge is improvement of the added noise in TWPA. One of the main phenomena, which could contribute to the noise, is capacitive dielectric loss. Losses become especially large when going to higher frequencies, as we are looking for when probing the axion mass in the range around 100 µeV, corresponding to a frequency of $\sim 25\,\text{GHz}$, at MADMAX. To further investigate their origin & to reduce them, $\lambda/2$-Josephson resonators were built to measure $\tan(\delta)$ via extraction of quality factors. Two different geometries were compared. For a close metallic ground, separated by a 22 nm layer of alumina, internal quality factors are found to be $Q_i = 216 \pm 22$ at single-photon level, corresponding to loss tangents of $\tan(\delta) \approx 5 \times 10^{-3}$. In the reference geometry without the close ground we find $\tan(\delta) \sim 10^4$.

Zusammenfassung

MAMDAX ist ein Experiment zur Suche nach dunkler Materie Axionen. Um die erforderliche Detektionssensitivität zu erreichen, werden Vorverstärker benötigt, die an oder nahe der Quantengrenze betrieben werden können. Parametrische Wanderwellenverstärker (TWPA) sind ein vielversprechendes Werkzeug, um dies im Frequenzbereich um 20 GHz zu erreichen. Um die Standardquantengrenze zu erreichen, besteht eine offene Herausforderung in der Verbesserung des zusätzlichen Rauschens in TWPA. Eines der Hauptphänomene, das zum Rauschen beitragen könnte, sind kapazitive dielektrische Verluste. Die Verluste werden besonders groß, wenn man zu höheren Frequenzen übergeht, wie wir sie bei einer Axionmasse im Bereich um 100 µeV, entsprechend einer Frequenz von ~ 25 GHz, bei MADMAX untersuchen. Es gilt daher ihren Ursprung weiter zu untersuchen um sie reduzieren zu können. Hierfür wurden $\lambda/2$-Josephson-Resonatoren gebaut, um $\tan(\delta)$ durch Bestimmen der Qualitätsfaktoren zu messen. Es wurden zwei verschiedene Geometrien verglichen. Für eine nahe metallische Erdung, getrennt durch eine 22 nm dicke Schicht aus Aluminiumoxid, ergeben sich interne Qualitätsfaktoren von $Q_i = 216 \pm 22$ im Bereich der Energien einzelner Phtotonen entsprechend Verlusttangenten von $\tan(\delta) \sim 5 \times 10^{-3}$. In der Referenzgeometrie ohne die nahe Erdung ergibt sich $\tan(\delta) \sim 10^4$.

Acknowledgements

Many people have contributed to this work in different ways. I want to thank Otmar Biebel for agreeing to be my supervisor at LMU. I would like to express my gratitude towards Béla Majorovits for supervising my work and for providing me with this exciting project in very versatile environments, for always offering his help and for the opportunities that I have been given.

The time spent at Institut Néel was incredibly fruitful and interesting. I want to thank Nicolas Roch and the whole group for welcoming me into their team. My thanks goes especially to Gwenael Le Gal for teaching me so much, leading the way through the steps of the project and by setting a great example of how to do research. A big thanks to Giulio Cappelli for helping with the project in a lot of ways. Thanks also to Luca Planat, Nicolò Crescini and the others for their helpful advice.

I want to thank Anton Ivanov for his helpful comments and for giving me my first introduction to the operation of a VNA as well as the understanding of the open booster system. Also thanks to Chang Lee for introducing me to cryostat wiring and simulations of the boost factor.

To be able to join Dagmar Kreikemeyer and Christoph Krieger on their trip to CERN was a very valuable learning experience. I want to thank them for my first hands on contact with cryogenics and for explaining and letting me follow the P200 cold tests.

Thanks to Olaf Reimann and Derek Strom for their constructive input and interest in my project.

Finally I would like to thank my friends and family for always supporting me throughout this time.

Contents

Chapter 1

Introduction and Overview

The nature of dark matter remains one of the big mysteries of our time. The efforts of MADMAX (MAgnetized Disk and Mirror Axion eXperiment) are aiming towards solving the dark matter and the strong CP problem by detecting axions [1]. As the expected power of the axion induced signal is very weak, in addition to a booster and a strong magnet, good amplifiers are needed to reach the required levels of sensitivity. The step going from standard low noise amplifiers to quantum limited amplifiers like TWPA would increase the paste at which the axion parameter space is explored. To probe the well motivated region of axion masses between $m_a = 40\,\mu\text{eV}$ and $400\,\mu\text{eV}$ the signal to be amplified is in the range of $10\,\text{GHz}$ to $100\,\text{GHz}$.

The first Josephson junction based amplification near quantum limited operation was reported about 35 years ago [2]. Due to the challenges arising with the required nano-fabrication methods it took until 2015 for the first demonstration of a quantum limited TWPA [3]. As of today, most TWPA devices operate at a frequency between $4\,\text{GHz}$ and $12\,\text{GHz}$ [4].

For the purposes of MADMAX the operating frequencies of these quantum limited amplifiers have to be increased up to $20\,\text{GHz}$ and beyond. However, as the frequency increases, the losses in TWPA become larger. Conductor and dielectric losses are believed to be the main factors limiting their performance [4]. It is therefore of prime importance to investigate them.

To measure the losses in TWPA in this work, we build microwave resonators which consist of a Josephson junction array fabricated in the same way as the junctions in a TWPA. With the extraction of quality factors from the resonances obtained in a transmission measurement the loss tangent can be determined. From a direct comparison of two resonator geometries with and without the close metallic ground on top of the resonator array, its effect on the losses is probed.

The purpose of chapter 2 is to motivate the experimental efforts of MADMAX in the search for dark matter axions and the improvement of the therefore essential detector technology by investigation of dielectric losses. In chapter 3 we review the basics of parametric amplification and introduce the idea of the Josephson junction based resonators to measure the losses via the extraction of quality factors. The fabrication process to build the devices is explained in chapter 4. In chapter 5 the experimental setup for the measurement of the resonators is briefly introduced. Chapter 6 mentions a few efforts to improve the understanding of the resonators through simulations. A calculation to estimate the unknown value of the capacitance, which couples the feedline to the resonator array, is presented. The procedure for the measurements, mentioning the parameters and also the method used for the data analysis is described in chapter 7. Finally the experimental results are presented in chapter 8.

Chapter 2

Motivation

Several astrophysical observations suggest the existence of dark matter (DM), which does not interact with ordinary matter via the electromagnetic interaction. The rotation curves of galaxies for example show higher velocities than what would be expected merely due to visible matter [5], while some galaxies would not even have formed. Evidence from gravitational lensing and the cosmic microwave background strongly suggests the existence of dark matter [6]. It is estimated to make up for about 85 % of the matter in the universe [7]. In efforts to explain the observed phenomena, many experiments aim to determine the nature of dark matter. Axions are among the best motivated candidates and would solve the strong CP problem as well as give insight on dark matter.

2.1 Strong CP Problem

In the Standard Model (SM) of particle physics, the Lagrangian of quantum chromodynamics (QCD) contains a CP violating term. CP-symmetry holds when the physical phenomena remain unchanged after performing a charge conjugation (C) and a parity transformation (P). The following term violates parity and time reversal (T). Since charge, parity, and time reversal symmetry (CPT) holds, it therefore also violates CP.

$$\mathcal{L}_\theta = -\frac{\alpha_s}{8\pi}\theta G^a_{\mu\nu}\tilde{G}^{a\mu\nu}\,, \tag{2.1}$$

where $G^a_{\mu\nu}$ denotes the QCD field-strength tensor and $\tilde{G}$ its dual. The coupling strength of strong interaction is given by α_s. The angle $\theta \in [0, 2\pi)$ consists of two contributions. One from the angle defining the QCD vacuum. The other one from the common phase in the quark mass matrix, ArgDet M_q. As the sum of these, the angle θ quantifies the degree of CP-violation in the term (2.1). Unless they cancel each other out exactly this would manifest itself in observable effects like the neutron electric dipole moment $d_n \propto \theta$. As experiments have shown [8][9], the upper bound is

$$\theta < 1.3 \times 10^{-10}\,. \tag{2.2}$$

The required *fine-tuning* for θ to be this close to zero is the so called *strong CP problem.*

2.2 The Axion

As a solution to the strong CP problem Peccei and Quinn (PQ) proposed a new theory [10][11] in which the vacuum energy density of QCD depends on θ and is minimized for $\theta = 0$. It introduces a chiral symmetry $U(1)_{PQ}$ and a scalar field which spontaneously breaks the symmetry at the PQ scale f_a, giving rise to a new low mass boson, the *axion*. The axion field is then related as $a(x) = \theta(x) f_a$, where f_a can also be understood as the decay constant. Its mass is given by [12]

$$m_a = 5.70\,\mu\text{eV}\left(\frac{10^{12}\text{GeV}}{f_a}\right). \tag{2.3}$$

The axion-photon interaction is given by the Lagrange density

$$\mathcal{L}_{a\gamma} = -\frac{g_{a\gamma}}{4} F_{\mu\nu}\tilde{F}^{\mu\nu} a, \tag{2.4}$$

with the axion field a and the coupling strength $g_{a\gamma}$. The EM field-strength tensor is denoted as $F_{\mu\nu}$ and its dual $\tilde{F}^{\mu\nu}$.

Expressed in terms of electric field $\boldsymbol{E}$ and magnetic field $\boldsymbol{B}$, (2.4) can also be written as

$$\mathcal{L}_{a\gamma} = g_{a\gamma} a \boldsymbol{E} \cdot \boldsymbol{B}\,, \tag{2.5}$$

with

$$g_{a\gamma} = -\frac{\alpha}{2\pi f_a} C_{a\gamma} = -2.04(3) \times 10^{-16}\text{GeV}^{-1}\left(\frac{m_a}{1\mu\text{eV}}\right) C_{a\gamma}\,, \tag{2.6}$$

where α is the fine structure constant. The parameter

$$C_{a\gamma} = 1.92(4) - \frac{\mathcal{E}}{\mathcal{N}} \tag{2.7}$$

depends on the ratio of the electromagnetic and color anomalies $\mathcal{E}/\mathcal{N}$ of the PQ symmetry, which varies with the axion model. For the most common models it is of order $\mathcal{O}(1)$.

Using the full Lagrangian of the axion-photon interaction, one can derive modified Maxwell equations, which account for the axion field [13].

In particular, the interaction in (2.5) enters as a current in the Ampère-Maxwell equation

$$\boldsymbol{\nabla} \times \mathbf{B} - \epsilon\dot{\mathbf{E}} = g_{a\gamma}\mathbf{B}\dot{a}\,, \tag{2.8}$$

for a medium with permeability $\mu = 1$ and permittivity ϵ. If an external magnetic field $\mathbf{B_e}$ is applied, the axion field sources an electric field

$$\mathbf{E}_a(t) = -\frac{g_{a\gamma}}{\epsilon}\mathbf{B}_e\, a(t)\,. \tag{2.9}$$

Now consider a dielectric interface with different permittivity on both sides, placed in a magnetic field (see fig. 2.1). Since the usual Maxwell equations remain unchanged, the boundary conditions for electric and magnetic fields ($\boldsymbol{E}_{\parallel,1} = \boldsymbol{E}_{\parallel,2}$ and $\boldsymbol{B}_{\parallel,1} = \boldsymbol{B}_{\parallel,2}$) hold. As the axion-induced electric field depends on ϵ (eq. 2.9), there would be a discontinuity at the interface with a change in dielectric material. To compensate for this, electromagnetic waves of frequency $\nu_a = m_a/2\pi$ are emitted [1]. The effect is the strongest when $\boldsymbol{E}_a$ and therefore $\boldsymbol{B}_e$ are parallel to the dielectric interface [15].

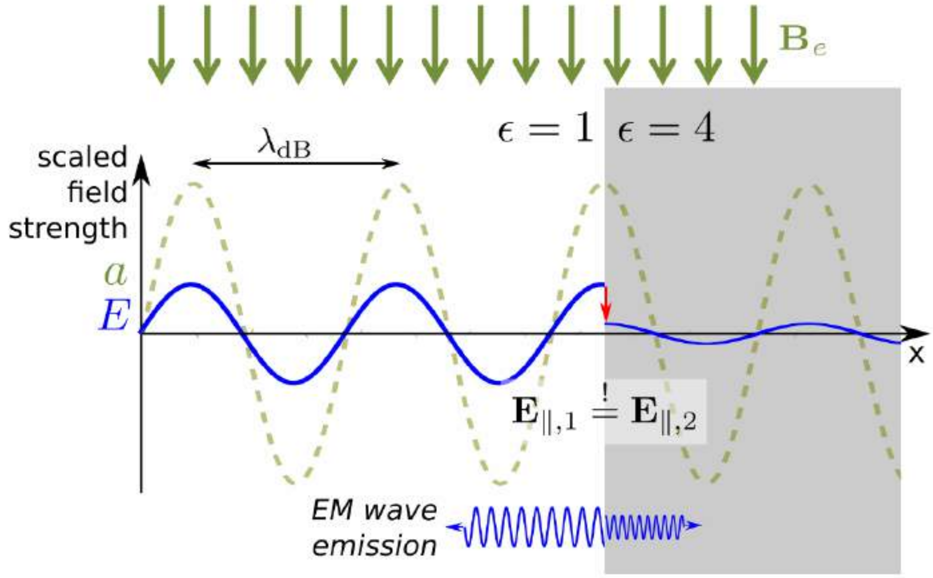

Figure 2.1: Axion induced EM field at dielectric surfaces in magnetic field. For clarity the emitted EM waves are shifted to the bottom of the figure. Taken from [14]

Axion dark matter: In the search for DM axions the astrophysical constraints that can be imposed on the parameter space vary depending on the way the axions are created. One method of axion creation is via the vacuum realignment mechanism[1]. The initial misalignment angle θ_i then determines the energy density of the axion field. In this case the axion can give the right amount of cold DM (CDM) and its properties are determined by the conditions when symmetry breaking occurs at the PQ scale. Furthermore there is a distinction between two scenarios: Whether the PQ symmetry breaking occurs before cosmic inflation (scenario A) or afterwards (scenario B). In scenario A, one patch inflates to the whole observable universe with the same θ_i. The PQ scale can have any value $f_a \gtrsim 10^9$GeV [16]. In scenario B, inflation happens before PQ symmetry breaking and there is patches of different θ_i in the observable universe. By considerations of statistical averages of the essentially random values in each causally disconnected patch, one can arrive at a prediction for the axion density as a function of f_a [17]. The mass range $26\,\mu\text{eV} \lesssim m_a \lesssim 1\,\text{meV}$ is then considered to be best motivated for the DM axion mass [18][19]. Assume $m_a \sim 100\,\mu\text{eV}$ and that the axions provide for the full local galactic CDM density of $(f_a m_a)^2\theta_0^2/2 \sim 300\,\text{MeV/cm}^3$. Taking the galactic virial velocity $v_a \sim \mathcal{O}(10^{-3})$ as the velocity dispersion on Earth and as the non-relativistic axion velocity. Then the axion de Broglie wavelenth is given by $\lambda_{\rm dB} = 2\pi/(m_a v_a) = 12.4\,\text{m}\,(100\,\mu\text{eV}/m_a)(10^{-3}/v_a)$. Therefore we expect the axion field to be a classical oscillating field $\theta \propto \theta_0 \cos(m_a t)$ with $\theta_0 \sim 4 \times 10^{-19}$. The expected frequency $\nu_a = m_a/(2\pi)$ is then in the microwave range [17].

Different approaches are being pursued to detect axions. Experiments based on cavity resonators in strong magnetic fields (Sikivie's haloscopes [20]) like ADMX [21], ADMX HF [22] or HAYSTAC [23] have good sensitivities for axion masses $m_a \lesssim 40\,\mu\text{eV}$. For even lower mass ranges, approaches using nuclear magnetic resonance techniques [24] and LC circuits [25] are being investigated. The mass range $m_a \gtrsim 40\,\mu\text{eV}$, which is highly attractive, is yet to be probed with experiments that have a high enough sensitivity to detect DM axions.

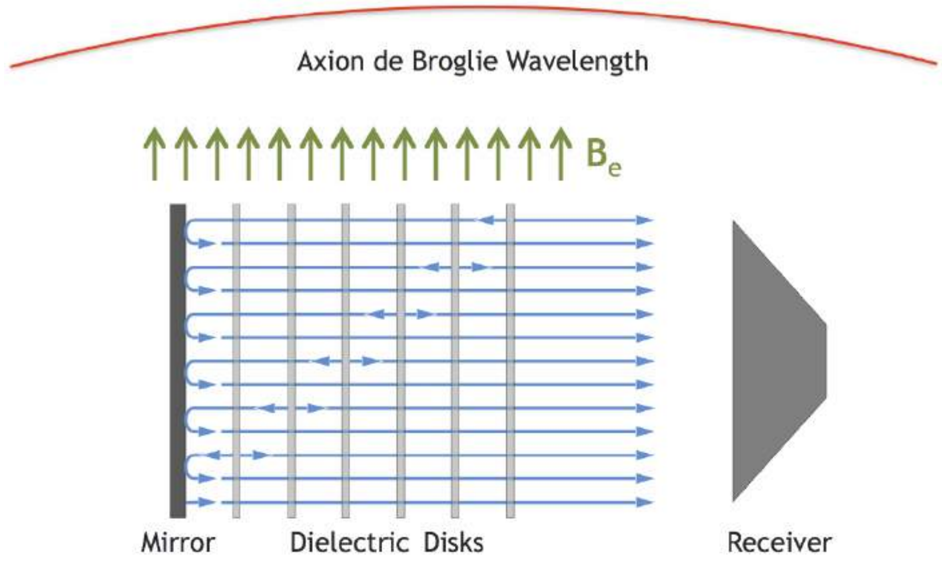

Figure 2.2: Booster overview with mirror, dielectric discs and receiver in an external magnetic field. The axion field is hinted at by the red line with a wavelength much bigger than the booster dimension. [1] [13]

2.3 Axion Search: MADMAX

The MAgnetized Disk and Mirror Axion eXperiment (MADMAX) is intended to search for axions in the mass range between 40 to 400 μeV, corresponding to frequencies from 10 to 100 GHz. The idea is to make use of constructive interference of axion induced EM waves emitted from multiple dielectric interfaces. By placing ~ 80 movable disks of lanthanum aluminate ($LaAlO_3$ with $\epsilon \approx 24$) of diameter $\sim 1.25\,\mathrm{m}$ and a thickness of $\sim 1\,\mathrm{mm}$ in a magnetic field $\boldsymbol{B}_e \approx 9\,\mathrm{T}$ and placing a mirror on one side - a *dielectric haloscope*. This *booster* system is shown in figure 2.2. The emitted radiation is then collected and measured by a receiver system. The setup is shown in figure 2.3. The distance in between the discs can be varied to adjust the conditions for constructive interference for different frequencies. This allows to scan through the range by changing the length of the booster from around 1.4 m at 10 GHz to 30 cm at 100 GHz. The booster is housed in a 4K cryostat to reduce noise by thermal radiation. The cryostat is surrounded by the dipole magnet.

The output power of the dielectric haloscope per unit area is [1]

$$\frac{P}{A} = \beta^2 \frac{P_0}{A} = 2.2 \times 10^{-27} \frac{\mathrm{W}}{\mathrm{m}^2} \left(\frac{B_e}{10\,\mathrm{T}} \right)^2 C_{a\gamma}^2 \,, \tag{2.10}$$

where β^2 is the power boost factor (the square of the amplitude boost factor β). $\beta^2 = P/P_0$ gives the power enhancement of the dielectric haloscope compared to just the output P_0 of a single magnetized mirror.

The boost factor $\beta(\nu_a)$ as a function of frequency can be estimated using a transfer matrix formalism [27]. It has been shown that the desired condition $\beta^2 \gg 1$ can be achieved in a frequency range by choosing the disk positions, even if the thickness of the disks is fixed. The behaviour of β^2 follows an area law. The integral $\int \beta^2 \, d\nu_a$ is approximately constant. Equality holds when the integration is performed over all frequencies and the approximation is good when the frequency range contains the main peak(s). Hence, there is a trade-off between a high boost factor and a wide frequency range (see fig. 2.4).

[1] Another way of axion creation is through reactions of SM particles in a thermal bath.

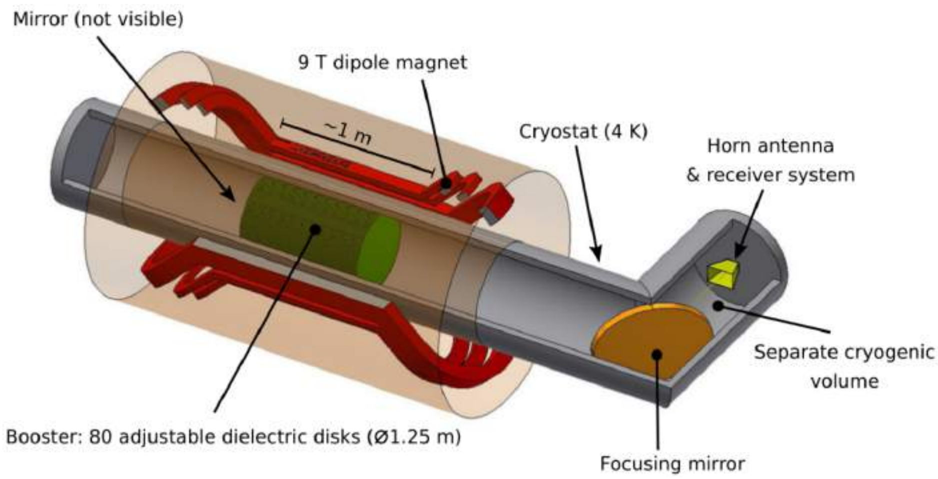

Figure 2.3: Design of MADMAX. [26]

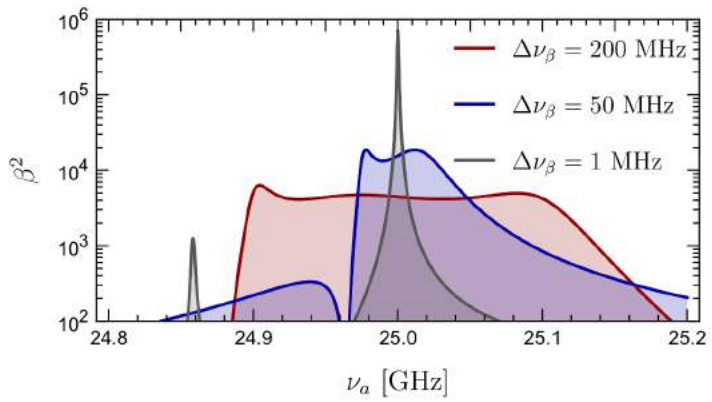

Figure 2.4: Power boost factor $\beta^2(\nu_a)$ for configurations of 20 dielectric disks($d = 1\,\mathrm{mm}$, $\epsilon = 25$), optimized for different frequency bandwidths $\Delta\nu_\beta$. [17]

In a setup with ~ 80 $LaAlO_3$ disks, a power boost factor of $\beta^2 \sim 5 \times 10^4$ can be achieved for a bandwidth of $\Delta\nu_\beta = 50\,\mathrm{MHz}$ at $\nu = 20\,\mathrm{GHz}$ [14]. When plugged into (2.3), this gives an emitted power per unit area of $P/A \sim 1.1 \times 10^{-22}\,\mathrm{W}$.

To be able to distinguish this small signal from thermal background noise, measurements are taken over some time τ. The signal power P_{sig} is integrated over the measurement time t_{scan}, for each frequency bin $\Delta\nu$. The sensitivity of the receiver, expressed as the signal-to-noise ratio (SNR) is given by the *Dicke radiometer equation* [28][29]

$$\frac{S}{N} = \frac{P_{\mathrm{sig}}}{k_B T_{\mathrm{sys}}} \sqrt{t_{\mathrm{scan}}\,\Delta\nu}\,, \tag{2.11}$$

with the Boltzmann constant k_B. The total system noise temperature is $T_{\mathrm{sys}} = T_{\mathrm{rec}} + T_{\mathrm{booster}}$ with a component from the receiver and the booster (and its surroundings). For the booster noise a few Kelvin can be assumed. In a setup using commercial high-electron-mobility transistor (HEMT) amplifier, the receiver noise is around $T_{\mathrm{rec}} \sim 6\,\mathrm{K}$

By switching to novel techniques like traveling wave parametric amplifiers (TWPA), the detection system noise might be reduced close to the quantum limit ($\sim 1\,\mathrm{K}$ at 20 GHz). Hence, this would also significantly reduce the system noise and therefore measurement times, which allows for a faster exploration of the axion parameter range.

2.4 Limitation for Detectors: Reaching Quantum Limited Amplification

To detect the very weak axion induced signal, low noise amplifiers with sufficient gain are needed. The power gain of an amplifier is given by

$$G = \frac{A_{\text{out}}^2}{A_{\text{in}}^2}, \tag{2.12}$$

with the signal input and output amplitudes $A_{\text{in/out}}$. It is commonly given in units of dB and is in general frequency dependent. The amplifier input consists of the signal and some noise, which will both be amplified. Additionally there will be some added noise coming from the amplifier itself. Firstly, environmental noise i. e. thermal noise and quantum noise from zero-point fluctuations. These can be reduced to a minimum of half a quantum (at the given frequency) by making use of a cryogenic environment. Secondly, there is intrinsic noise to the amplifier, also limited by quantum mechanics.

Let us briefly discuss this limit. Consider the input field with operator $\hat{a}_{\text{in}}$ entering the amplifier. Then the output field is given by

$$\hat{a}_{\text{out}} = \sqrt{G}\hat{a}_{\text{in}} \,. \tag{2.13}$$

The operators must follow the commutation relation

$$[\hat{a}_{\text{in}}, \hat{a}_{\text{in}}^\dagger] = [\hat{a}_{\text{out}}, \hat{a}_{\text{out}}^\dagger] = 1 \,. \tag{2.14}$$

For eq. (2.13) to hold with the condition of eq. (2.14) an aditional degree of freedom has to be added. There are now two cases: If the signal phase is this additional term, the amplifier is called *phase-sensitive*. Otherwise it is called *phase-preserving*.

As stated by Caves theorem, for a phase-preserving amplifier there has to be an additional internal mode $\hat{b}$ with $[\hat{b}, \hat{b}^\dagger] = 1$, called *idler* [30]. Through the interaction of the internal mode and the internal signal the output is produced. Since the idler and the input mode fluctuations are not correlated, Eq. (2.13) with the additional mode becomes

$$\hat{a}_{\text{out}} = \sqrt{G}\hat{a}_{\text{in}} + \sqrt{G-1}\,\hat{b}^\dagger \,. \tag{2.15}$$

The total noise power spectral density (PSD) for the amplifier output at signal frequency is [31]

$$\mathcal{N}_{\text{out}} = \frac{1}{2}\Big\langle \Big\{ \hat{a}_{\text{out}}, \hat{a}_{\text{out}}^\dagger \Big\} \Big\rangle \,. \tag{2.16}$$

By plugging in Eq. (2.15) the result is

$$\mathcal{N}_{\text{out}} = G\mathcal{N}_{\text{in,s}} + (G-1)\mathcal{N}_{\text{in,id}} \,, \tag{2.17}$$

with the signal and idler input noises $\mathcal{N}_{\text{in,s}}$ and $\mathcal{N}_{\text{in,id}}$, respectively. It is then clear, that only for $G \approx 1$ the idler mode does not add additional noise. This, however, would also render the amplifier pointless. A very small gain is not enough to amplify the signal to a level where we do not have the quantum mechanical constraints on the minimal noise. For $G \gg 1$ the noise referred to the input is given by

$$\frac{\mathcal{N}_{\mathrm{out}}}{G} \cong \mathcal{N}_{\mathrm{in,s}} + \mathcal{N}_{\mathrm{in,id}} \,. \tag{2.18}$$

The term $\mathcal{N}_{\mathrm{in,id}}$ is thus the added noise directly coming from the idler mode of the phase preserving amplifier. (For phase-sensitive amplification only one of the quadratures is amplified while the other one is squeezed. The phase-space volume remains constant.)

As a result of environmental and amplifier noise (both add half a quanta), the standard quantum limit (SQL) of noise is defined as 1 quantum of energy. In units of temperature it is expressed as [30]:

$$T_{\mathrm{SQL}} = \frac{h\nu}{k_B} \tag{2.19}$$

The detection system for very low amplitude signals usually has several amplifiers connected in series. This amplification chain e. g. consists of 2 amplifiers. One with noise temperature $T_{N,1}$, followed by another one with noise temperature $T_{N,2}$. It has the total noise

$$T_{N,\mathrm{chain}} = T_{N,1} + \frac{T_{N,2}}{G_1} \,. \tag{2.20}$$

Hence, the total noise of an amplification chain will almost entirely depend on the quality of the first amplifier (preamplifier) if the gain is sufficiently high. The aim is therefore to reach SQL noise and a Gain of $G_1 \sim 20$ dB at the preamplifier. In comparison: high-electron-mobility transistors (HEMT) [32] typically have noise levels at around ~ 5 SQL [33]. Due to their dissipative nature they can not be operated at millikelvin temperatures and are usually placed at 4 K. To get close to SQL, travelling wave parametric amplifiers (TWPA) can be used. The amplifiers with the lowest noise built so far (while still having a good gain ~ 20 dB) were able to reach a noise level as low as 2 times SQL[3]. Their operating frequencies are mostly in the microwave frequency range between 4 to 12 GHz. For these frequencies, operation of amplification chains based on Josephson parametric amplifiers has already been demonstrated in other axion search experiments.[34][23] For MADMAX however, TWPA working at frequencies of 20 GHz and higher are needed to explore the desired axion mass ranges. One of the main limiting effects are thought to be dielectric losses. They come from the dielectric, which is used to impedance match the TWPA to 50 Ω [4]. The goal of this work is to investigate the cause of these losses further by measuring them in a resonator geometry, similar to one that can be used in TWPA.

2.5 Improvement of Dielectric Losses in substrates at High Frequencies

The TWPA devices that we are considering, consist of an array of Josephson junctions (see Sec. 3.1), and can be seen as microstrip ([35]) transmission lines. As such, they are subject to different loss mechanisms, namely conductor and dielectric loss. For superconductors and thick metallic grounds, the conductor losses might be assumed to be negligible. However, in the device geometry we are considering (see chapter 4) the metallic ground is not superconducting and its thickness is comparable to its skin depth [36]

$$\delta_s = \sqrt{\frac{2}{\omega\mu_0\sigma}} \,, \tag{2.21}$$

where $\omega/2\pi$ is the frequency of the microwave, μ_0 the vacuum permeability and σ the conductor conductivity.

We can model the total attenuation of the transmission line with length L as [37]

$$A = e^{(\alpha_c+\alpha_d)L} \tag{2.22}$$

with dielectric loss depending on the wave vector k as

$$\alpha_d = \frac{k \tan\delta}{2}\,. \tag{2.23}$$

The loss tangent quantifies the energy that is dissipated, when an electromagnetic wave propagates through a dielectric. It is given as

$$\tan(\delta) = \frac{\epsilon''}{\epsilon'}, \tag{2.24}$$

where ϵ' and ϵ'' are the real and imaginary part of the permittivity ϵ of the dielectric medium.

The conductor losses can be modeled as

$$\alpha_c = \frac{R_s}{Z_c W}\,, \tag{2.25}$$

with the width of the transmission line W, the characteristic impedance of the line Z_c and the surface resistivity R_s. The surface resistivity is independent of the conductor thickness t for $t \gg \delta_s$. But in the case where they are comparable, the effective surface resistivity is higher. We can model the conductor loss as $\alpha_c = L_c\sqrt{\omega/(2\pi)}$ with a parameter L_c accounting for the conductor loss.

In this model we notice that, due to the linear and square root dependence on the signal frequency, the dielectric loss dominates for higher frequencies and conductor loss affects the lower frequencies. [36] Aiming for TWPA operating at the SQL and higher frequency, their losses have to be further investigated.

In this work, the approach follows up on the idea in [38]. Resonators made with the same fabrication techniques that are also used to build TWPA, are used as a reference device to measure losses more precisely. Their losses, and therefore the TWPA losses, can be measured through another concept known from resonator theory.

2.5.1 Quality Factors

Consider a microwave resonator with some capacitance, which consists of a lossy dielectric with complex permittivity ϵ. The resonator will dissipate energy over time. In this sense it is possible to relate the loss tangent and a dissipation factor or the inverse of the (internal) *quality factor* as

$$\tan(\delta) = \frac{1}{Q_i}. \tag{2.26}$$

This quality factor Q_i is a characteristic of the resonator itself and does not take into account any loading effects from external circuitry. When considering the measuring apparatus, there is another contribution which arises from the coupling of the resonator to this circuitry. The effect is that the overall Q_L (loaded quality factor) is lowered. [37] An external quality factor

Q_e can be defined to account for this contribution. The expression for the loaded quality factor then reads

$$\frac{1}{Q_L} = \frac{1}{Q_i} + \frac{1}{Q_e}\,. \tag{2.27}$$

It is important to investigate how dielectric loss in a material changes with the power of the electromagnetic waves. For Temperatures below $\sim 1\,\mathrm{K}$ it has been observed that for high intensities ($\sim \mathcal{O}(10)\mathrm{W/cm^2}$) the losses become very small (e. g. $\tan(\delta) < 10^{-5}$ for vitreous silica at 10 GHz)[39]. In the context of superconducting qubits or LC resonators made from superconducting components like Josephson junctions, dielectric losses act as the main source of quantum decoherence. The dielectric losses are not well defined in the low power low voltage regime. It is observed to scale inversely proportional to the excitation voltages in these qubits. When further decreasing the voltages it tends to level off at an intrinsic value (see Chapter 8). This behaviour has been postulated to arise from coupling of the radiator to a *bath* of two-level state (TLS) defects. They absorb and disperse energy at low power but are saturated at higher voltages and temperatures. For that reason it is typical for TLS-induced loss to show an increase in loss with a decrease in excitation voltage. [40] [41]

Chapter 3

Detection Technology: Josephson Parametric Amplification and TWPA

In this chapter, first the Josephson Junction as the building blocks for the implementation of parametric amplifiers will be reviewed. Then, a few examples of parametric amplification will be outlined, leading to traveling wave parametric amplifiers (TWPA). Finally, the resonators used to measure losses to investigate the limiting factors of TWPA, are introduced.

3.1 Josephson junctions

As the building blocks of the quantum limited amplifiers, we use Josephson junctions. They are a great candidate, since they can be used for parametric interaction ,work at cryogenic temperatures and are superconducting.

A Josephson junction consists of two superconductors closely separated by an insulating layer. Cooper pairs can tunnel through this thin barrier. Due to a difference in the phase of the macroscopic wave function of the electrons in the superconductors, this results in a supercurrent [42]

$$I_s = I_c \sin(\phi_2 - \phi_1). \tag{3.1}$$

I_c is called the *critical current* and is the maximum current that can flow through the junction up to which the superconducting properties of the junction are preserved. The effect was predicted by Brian D. Josephson in 1962 [43]. If a voltage V is applied to the leads of the junction, the phase difference evolves with time according to

$$\frac{d}{dt}(\phi_2 - \phi_1) = \frac{2e}{\hbar}V = \frac{2\pi}{\Phi_0}V, \tag{3.2}$$

where $\Phi_0 = \frac{h}{2e}$ is the magnetic flux quantum. From the second Josephson equation 3.2 we see, that for a constant voltage the phase difference will increase linearly with time. There will be an AC current with frequency $f = \frac{V}{\Phi_0}$.
This allows for modeling the Josephson junction as a perfect nonlinear element with kinetic inductance L_J. Kinetic, since there is no associated magnetic field. The behaviour instead stems from the kinetic energy of the charge carriers, the Cooper pairs.

Apply the chain rule and use Eqs. 3.1 and 3.2 to calculate the time derivative of the Josephson supercurrent

$$\frac{\partial I}{\partial t} = \frac{\partial I}{\partial \phi}\frac{\partial \phi}{\partial t} = I_c \cos\phi \cdot \frac{2\pi}{\Phi_0}V. \tag{3.3}$$

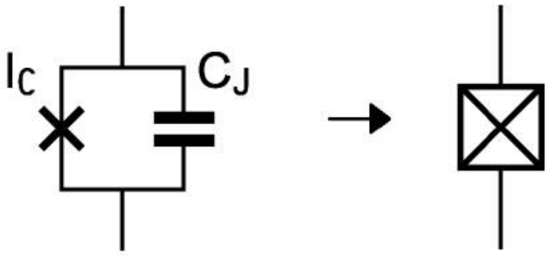

Figure 3.1: Circuit diagram of a Josephson junction consisting of a capacitor and a perfect nonlinear element. The compact notation is shown on the right.

Comparing with the current-voltage characteristic of an inductor

$$V = L(\phi)\frac{\partial I}{\partial t} \tag{3.4}$$

one ends up with the inductance

$$L(\phi) = \frac{\Phi_0}{2\pi I_c \cos\phi} = \frac{L_J}{\cos\phi}, \tag{3.5}$$

where

$$L_J = L(0) = \frac{\Phi_0}{2\pi I_c} \tag{3.6}$$

is called the Josephson inductance. It is the linear part of the inductance. The nonlinear dependence of the inductance with respect to power is the essential part for its use as the elementary building block in parametric amplifiers. [38]

To finish the modeling of the Josephson junction, also consider the capacitive effect between the superconducting leads. This capacitance can be modeled by a parallel plate capacitor C. Then the junction is represented by a nonlinear LC circuit with resonant angular frequency

$$\omega_\Pi = \frac{1}{\sqrt{L_J C}}. \tag{3.7}$$

For the fabrication process used the value for the Josephson junction capacitance per area is $C = 45\,\mathrm{fF/\mu m^2}$ [44]. With values for the junction area similar to the one used in this thesis (see chapter 4) we estimate the resonant frequency of these junctions to be around $\sim 20\,\mathrm{GHz}$.

The commonly used notation for a Josephson junction in an electric circuit diagram is shown in Fig. (3.1). [45]

3.2 Parametric Amplification

3.2.1 Introductory Example: Person on a Swing

To get familiar with the concept, let us first consider an example of classical parametric amplification. A person is standing on a swing (see Fig. 3.2), periodically modulating their center of mass (CM) by standing up and crouching. If the CM is fixed, the motion is described by the angular displacement

$$\theta(t) = \theta(0)\cos(\omega_s t) + \frac{L(0)}{m\omega_s l}\sin(\omega_s t)\,, \tag{3.8}$$

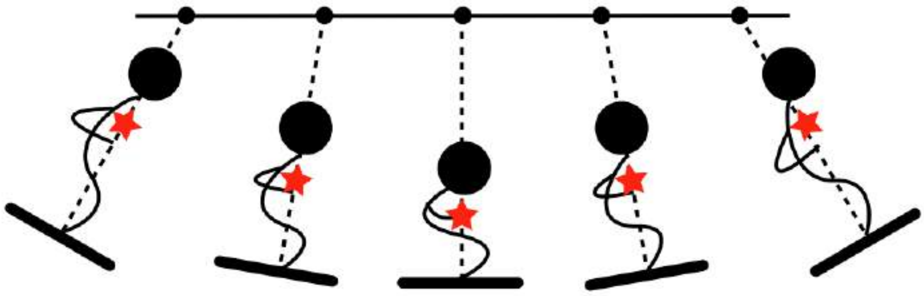

Figure 3.2: Visualization of parametric amplification by motion of a person on a swing. The amplification is driven by changing the center of mass (red star) by standing and crouching. In other words, changing the effective length of the pendulum at twice the frequency of the unperturbed swing. From [46]

where $L(0)$ and $\theta(0)$ are the initial angular momentum and initial angular displacement of the swing. The pendulum mass and length are given by m and l. Now the CM and therefore the effective length of the swing is modulated. The effective length becomes a periodically modulated parameter, therefore the interaction is called parametric. Then the resonance frequency of the swing $\omega_s = \sqrt{g/l}$ (g is the usual standard acceleration due to gravity) becomes

$$\omega_s(t) = \omega_s(0) + \epsilon \sin(\omega_p t)\,, \tag{3.9}$$

with the unperturbed swing frequency $\omega_s(0)$ and the (perturbing) CM modulation frequency ω_p. The resulting frequency change of the swing is given by ϵ. In the case where the CM is modulated with frequency $\omega_p = 2\omega_s$ the solution of the equation of motion is

$$\theta(t) = \theta(0)e^{\epsilon t/2}\cos(\omega_s t) + \frac{L(0)}{m\omega_s l}e^{-\epsilon t/2}\sin(\omega_s t)\,. \tag{3.10}$$

The oscillator absorbs energy from the parametric driving motion at a rate proportional to the energy it already has. If there is no compensating energy-loss mechanism as in the considered case, the initial amplitude is exponentially amplified, while the out-of-phase component is exponentially suppressed. If there is no initial displacement of the swing from the equilibrium position ($\theta(0) = L(0) = 0$) there will be no amplification. It is intuitively clear in this example, as one cannot transfer angular momentum by standing up and crouching on a swing that is standing still. Setting position and momentum to zero is not forbidden in classical mechanics. It is however, when going to a quantum mechanical oscillator. [46][47]

3.2.2 Basics of Parametric Amplification

From a quantum optics viewpoint the process is the following: In a parametric interaction electromagnetic (EM) waves of different frequency mix and generate an EM wave with another frequency. An example is *spontaneous parametric down conversion* (SPDC), where a high amplitude EM wave with frequency $\omega_p/2\pi$, called pump, enters a nonlinear medium and generates two EM waves of lower frequencies $\omega_s/2\pi$ (signal) and $\omega_i/2\pi$ (idler), in accordance with conservation of energy and momentum. Amplification can be achieved when signal and pump are sent towards the nonlinear medium (e.g. the polarization in the medium is a nonlinear function of the electric field). The pump induces a periodic change in the refractive index and therefore the wave velocity, which leads to a transfer in energy from the pump to the

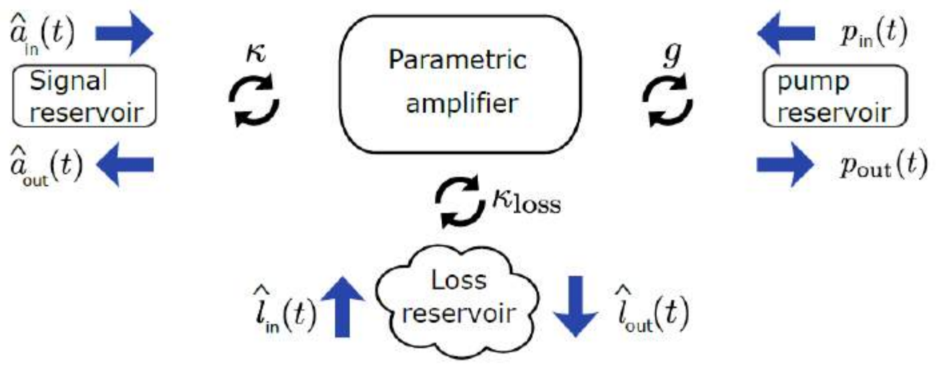

Figure 3.3: The different contributions to resonant parametric amplification. From [38]

signal mode via creation of the idler mode.[1] To get parametric amplification of microwaves, the nonlinear inductance of superconducting circuits like Josephson junctions is used as the nonlinear medium.

To enhance the amplification of the signal, the interaction time in the nonlinear medium has to be increased. This can be achieved using resonant amplification by placing the nonlinear medium in some sort of a cavity. The interaction time will then be the inverse of the cavity line width. However, this puts a constraint on the amplification bandwidth, since it also depends on the cavity line width. The other approach are traveling wave amplifiers, where the interaction time is increased with the physical length of the nonlinear medium. [4][38]

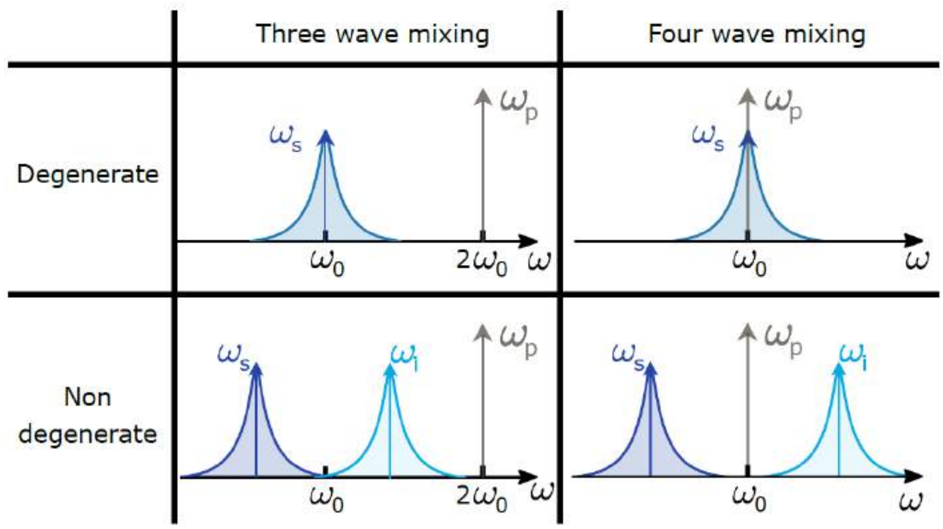

Figure 3.4: Different configurations of parametric amplification. The amplification can be a 3 wave mixing ($\omega_p = \omega_s + \omega_i$) or 4 wave mixing ($2\omega_p = \omega_s + \omega_i$) process. In the degenerate case signal and idler share the same spatial mode. From [38]

For resonant parametric amplification the amplifier, consisting of the resonator and the non-linear medium, can be understood as a nonlinear resonator (NLR) with resonant frequency $\omega_0/2\pi$ (which is different to the resonant frequency without the nonlinear medium). It is coupled to different ports (see Fig. 3.3). If the amplification is happening in reflection, the signal input $\hat{a}_{\text{in}}(t)$ and ouput field $\hat{a}_{\text{out}}(t)$ share the same port with damping rate κ. Losses can be modelled through the coupling to a loss reservoir with rate κ_{loss}. The pump is coupled to the amplifier through another port with damping rate g. The NLR intra-resonator field is

[1] Note that in the classical example of the swing the idler mode was not needed for a transfer in energy.

described by its creation operator $\hat{a}^\dagger$ and annihilation operator $\hat{a}$.

In (Fig. 3.4) different possible processes for parametric amplification are shown, which have to be distinguished. For a *three wave mixing* process (3WM), one pump photon gives one signal and one idler photon, related by $\omega_p = \omega_s + \omega_i$. In the case of *four wave mixing* (4WM), two pump photons give one signal and one idler photon. Furthermore, if signal and idler share the same spatial mode, the amplifier is called *degenerate*. If the idler evolves in a spatially separated mode, it is *non-degenerate*. [38]

3.2.3 Four Wave Mixing

For the example case of 4WM degenerate amplification, the situation is the one of a pump oscillator coupled with rate g to a nonlinear resonator. As the pump field has a large amplitude, it can be described by a classical drive with frequency $\omega_p/2\pi$ and field amplitude p. The position and momentum of this drive oscillator are

$$X_p = x_p(p + p^*) \quad \text{and} \quad Y_p = -iy_p(p - p^*) \tag{3.11}$$

with their respective amplitudes x_p and y_p and associated potential and kinetic energies U_p and T_p. The nonlinear oscillator however is described by the position and momentum operators

$$\hat{X}_a = x_a^{\text{zpf}}(\hat{a} + \hat{a}^\dagger) \quad \textit{and} \quad \hat{Y}_a = -iy_a^{\text{zpf}}(\hat{a} - \hat{a}^\dagger)\,, \tag{3.12}$$

with the zero-point fluctuations x_a^{zpf} and y_a^{zpf} respectively. The potential and kinetic energies are U_a and T_a and ω_0 its resonant frequency

The potential of the NLR expanded to fourth order is

$$\begin{aligned} U_a(t) &= -U_a^0 \cos\left(x_a^{\text{zpf}}\left(\hat{a} + \hat{a}^\dagger\right)\right) && (3.13)\\ &\approx -U_a^0\Big[1 - \frac{1}{2!}\left(x_a^{\text{zpf}}\left(\hat{a} + \hat{a}^\dagger\right)\right)^2 + \frac{1}{4!}\left(x_a^{\text{zpf}}\left(\hat{a} + \hat{a}^\dagger\right)\right)^4\Big]\,. && (3.14) \end{aligned}$$

The pumped Hamiltonian is given by [48][49]

$$\hat{H}_{\text{4WMD}} = \hbar\omega_p p^* p + \hbar\omega_0 \hat{a}^\dagger \hat{a} - U_a^0 \hat{a}^{\dagger 2}\hat{a}^2 + \hbar g(p + p^*)(\hat{a} + \hat{a}^\dagger)\,. \tag{3.15}$$

It can be rewritten (and simplified) in the form

$$\frac{\hat{H}_{\text{4WMD}}}{\hbar} = \Omega \hat{a}^\dagger \hat{a} + \frac{\lambda}{2}\hat{a}^{\dagger 2} + \frac{\lambda^*}{2}\hat{a}^2\,, \tag{3.16}$$

with the frequency Ω of the rotating frame we study the system in

$$\Omega = \omega_0 - \omega_p + 2K|\alpha|^2\,, \tag{3.17}$$

and the pump strength λ given by

$$\lambda = K\alpha^2\,, \tag{3.18}$$

with *Kerr* coefficient $K = -2U_a^0/\hbar$ that quantifies the nonlinearity. It produces a power dependent phase shift, similar to the optical Kerr effect. The pump amplitude of the resonator is denoted α.

To get an expression for the gain of the resonant parametric amplifiers, one has to solve the quantum Langevin equation (QLE) for $\hat{a}(t)$ with the derived expression of the Hamiltonian. As it turns out, the term $\Delta_{\mathrm{bw}}\sqrt{G_{\mathrm{max}}} = \kappa$ is a constant, which reflects an inherent property of resonant parametric amplifiers, that there is always a tradeoff between maximum gain G_{max} and frequency bandwidth Δ_{bw}. A more detailed treatment and full derivation of the Hamiltonians for the different amplification processes is given in [38].

3.2.4 The Kerr Nonlinearity

Coming from nonlinear optics, the polarization to a strong electric field in a nonlinear medium is described by

$$\mathbf{P} = \epsilon_0 \left(\chi^{(1)} \cdot \mathbf{E} + \chi^{(2)} : \mathbf{EE} + \chi^{(3)} \vdots \mathbf{EEE} + ... \right) , \tag{3.19}$$

with ϵ_0 being the vacuum permittivity and $\chi^{(n)}$ the n-th order component of the electric susceptibility of the medium. The dot symbols represent scalar products between matrices. In a dielectric medium, the linear refractive index is

$$n_{\mathrm{L}} = \sqrt{\epsilon_r} = \sqrt{1 + \chi^{(1)}} \tag{3.20}$$

with relative permittivity ϵ_r. Since $\chi^{(2)}$ often vanishes, the first nonlinear term is $\chi^{(3)}$. The refractive index can then be written as

$$n = n_{\mathrm{L}} + \frac{3}{8n_{\mathrm{L}}}\chi^{(3)} |\mathbf{E}|^2 . \tag{3.21}$$

The shift of the refractive index for light evolving in such a nonlinear medium, causes a phase shift. If the phase shift is induced by the light beam itself, it is called self-phase modulation (SPM). When it is due to another beam, it is called cross-phase modulation (XPM).

Transferring this concept to Josephson-based resonators, the Kerr effect induces a shift of the resonance frequency. With the Josephson potential for a nonlinear resonator in a 4WM process (Eq. 3.13), the Hamiltonian without pumping is

$$\frac{\hat{H}_{\mathrm{Kerr}}}{\hbar} = (\omega_0 - K\hat{a}^\dagger\hat{a})\hat{a}^\dagger\hat{a} \, , \tag{3.22}$$

with $K = 4U_0/\hbar$. The resonance shifts because of the $K\hat{a}^\dagger\hat{a}$ term. For higher powers it shifts to lower frequencies. In this context one also speaks of self and cross Kerr effect. If there is an additional pump field like in the case of 4WMD amplification from earlier, the resonance is shifted due to the pump amplitude $|\alpha|^2$ (cross-Kerr). Saturation of the amplification happens when the signal power becomes large enough to shift the resonance even further to a point where the pump frequency is off resonance. It is usually given in terms of the 1 dB compression point. The power at which the gain drops by 1 dB.

3.2.5 Going to Traveling Wave Amplifiers

Implementation: To discuss the implementation of a Kerr-based amplifier (4WMD) with a Josephson junction, one can switch from the quantum optics to the quantum circuits formalism. As seen in section 3.1, Josephson junctions can be modeled as anharmonic LC circuits. Such a circuit with inductance L and capacitance C can be discribed by the Hamiltonian

$$\hat{H} = \frac{\hat{Q}^2}{2C} + E_J \cos\left(\frac{\hat{\Phi}}{\phi_0}\right) \tag{3.23}$$

with the reduced magnetic flux quantum $\phi_0 = \hbar/(2e)$ and the Josephson potential $E_J = \phi_0^2/L$ with elementary charge e.

A direct analogy can be made between a nonlinear resonator and a Josephson junction. The generalized flux $\hat{\Phi}$ and the charge $\hat{Q}$ correspond to the position $\hat{X}$ and momentum $\hat{Y}$ respectively. They can be written as

$$\hat{\Phi} = \sqrt{\frac{\hbar}{2\omega_0 C}}(\hat{a} + \hat{a}^\dagger) = \phi_{\text{zpf}}(\hat{a} + \hat{a}^\dagger) \tag{3.24}$$

$$\hat{Q} = -i\sqrt{\frac{\hbar\omega_0 C}{2}}(\hat{a} - \hat{a}^\dagger) = -iq_{\text{zpf}}(\hat{a} - \hat{a}^\dagger)\,, \tag{3.25}$$

with the resonant angular frequency of the junction $\omega_0 = 1/\sqrt{LC}$.

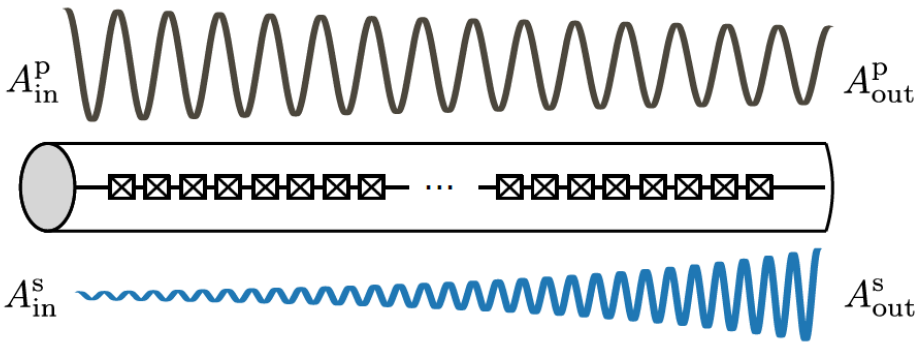

Figure 3.5: Sketch of traveling wave parametric amplification. Signal and pump are travelling through the amplification chain of Josephson junctions (from left to right). Energy is transferred to the signal mode. [38]

TWPA: The interaction time in the nonlinear medium can also be increased by using traveling wave amplification in a transmission line of long physical length. As it has been shown, the gain-bandwidth constraint of resonant amplification can be overcome. The amplification process is sketched in Fig. 3.5. The modes are traveling through the medium and the signal amplitude is amplified as the waves propagate forward.

A problem that arises is a phase mismatch between the different modes in the transmission line. This comes from the curved dispersion relation and a mismatch caused by self and cross phase modulation, which makes the pump travel with higher phase velocity than signal and idler. This total phase mismatch limits the maximum gain of the amplifier. There is different approaches to solve this. It is possible to engineer a gap in the dispersion relation (e.g. by periodic patterns in the junction properties or by resonant elements along the metamaterial). Then the phase matching condition can be fulfilled when the pump frequency is close to this gap. Another approach is to get phase matching, bases on a sign reversal of the Kerr nonlinearity, so that both contributions cancel each other out [50]. This can be achieved by using different asymmetric unit cells containing more than one Josephson junction, allowing to tune the three and four wave mixing nonlinearities with a magnetic field.

Another challenge is to impedance match the array of the TWPA. The ends of the transmission line are connected to standard microwave transmission lines with an impedance of $Z_0 = 50\,\Omega$. The characteristic impedance of the array is given by

$$Z_C = \sqrt{\frac{L_J}{C_g}} \tag{3.26}$$

with the Josephson junction inductance L_J and their capacitance to ground C_g. As L_J is very large, it has to be compensated by a large capacitance per unit length. This can be achieved by placing a metallic ground close to the junction array, which significantly increases C_g. It is separated by a dielectric and the distance can be chosen to get the impedance of the array match Z_0.

3.3 Josephson $\lambda/2$-Resonator

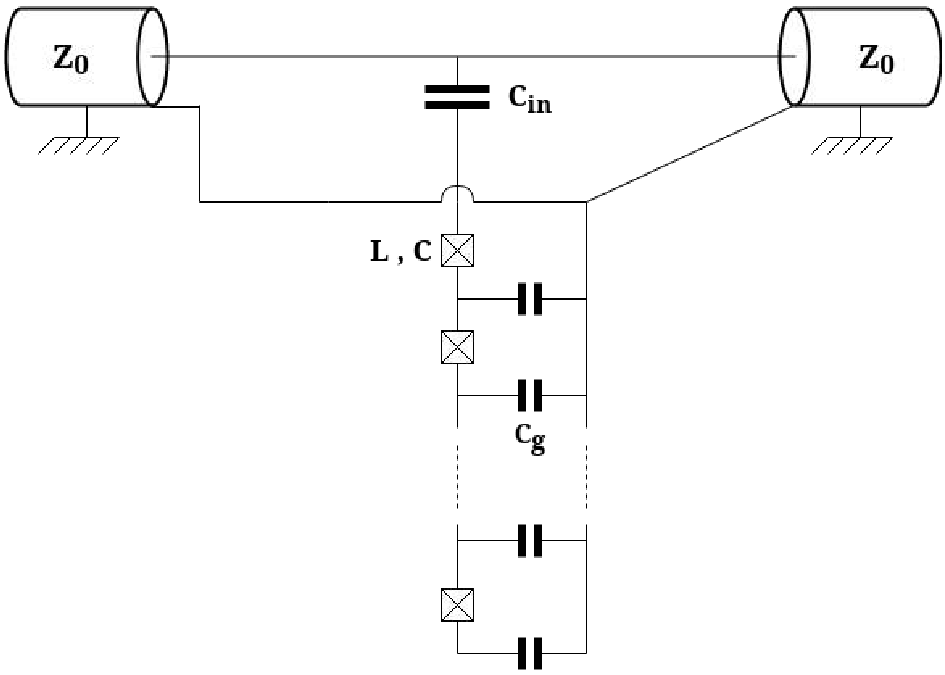

Figure 3.6: Circuit diagram of the $\lambda/2$ resonator. The resonator consists of an array of Josephson junctions and is capacitively coupled to a $50\,\Omega$ transmission line.

As losses are thought to be a major factor, which limits the performance of TWPA at higher frequencies, their nature still has to be fully understood to mitigate them. In a device geometry with a very close metallic ground for impedance matching, the losses are thought to come mainly from the dielectric in between this close ground and the Josephson junction (JJ) array. In this area the electric field density is much higher than to the far away ground on the other side of the silicon wafer, the JJ array is written on (see Chap. 4). As mentioned in Sec. 2.5, the losses in the array can be investigated via the use of resonators. The original motivation in [38] was to use them as a control sample and the idea to use them as a Q_i meter is developed in [51]. By inferring the dielectric loss from the extraction of the quality factor (procedure described in Sec. 7.2), it can be compared to the results obtained by directly measuring the transmission of a Josephson transmission line. Using the resonators, the result can also be more precise and give further insight on the nature of contributions to the losses.

The resonators in this work are constructed in a so called hanger geometry as shown in Fig. (3.6). A microwave transmission line (*feedline*) of impedance $Z_0 = 50\,\Omega$ in a coplanar waveguide (CPW) geometry is coupled to the resonator, which consists of a an array of $N = 600$ Josephson junctions. The coupling is done with a capacitor C_{in}, which is implemented as an interdigitated (finger) capacitor. The JJs in the array are described by heir Josephson inductance L (see 3.1) and the Josephson capacitance which, for the process used, has a value per area of $C/A \approx 45\,\text{fF}\,\mu\text{m}^{-2}$ [44][38]. As such, the resonator array can be understood as a series of LC circuits.

Additionally, each junction is capacitively coupled to the metallic ground, quantified by C_g. In the case of the close ground separated by a thin dielectric film of thickness t_d on top of the array, it can simply be modeled as a parallel plate capacitor

$$C_g = \epsilon_0 \epsilon_r \frac{A_{tot}}{t_d}\,, \tag{3.27}$$

with relative permittivity ϵ_r (≈ 9.8 for the used aluminum oxide, also called *alumina*) and the area of a unit cell of the array (containing a junction and a connecting wire).

For the resonator array of length $\ell = Na$ (with a the length of a unit cell), the resonance condition is given by the boundaries (C_{in} and an open end), as

$$\ell = n\,\frac{\lambda_n}{2} \quad , n \in \mathbb{N}\,. \tag{3.28}$$

It behaves like a parallel resonant circuit with resonant modes of wavelength λ_n. [37]

Two different types of resonators have been built and are compared in this thesis. Type 1 has the close metallic ground deposited right on top of the junction array. In this case C_g is predominantly influenced by the close ground on top of it (called *top ground*). For type 2, there is no top ground above the junction array. Instead it is next to it in a coplanar geometry. The capacitance of the junctions to ground is therefore expected to be much lower. One way can be to model it as two parallel coplanar strips (pcs), which gives

$$C_{g,\text{pcs}} = \epsilon_0 \epsilon_r l\,\frac{K(\sqrt{1-k^2})}{K(k)}\,, \tag{3.29}$$

with l being the length of the parallel conducting strips and K the elliptic integral of the first kind [52]. The argument is defined as $k = \sqrt{k_1 k_2}$ with

$$k_{1/2} = \left(\frac{2w_{1/2}}{d} + 1\right)^{-1}\,, \tag{3.30}$$

where w_1 and w_2 are the strip widths.

Chapter 4

Resonator Fabrication

This chapter aims to describe all the required steps in the fabrication process of the resonator devices. The procedures were conducted at *Institute Néel* of the *French National Centre for Scientific Research (CNRS)* in Grenoble. Except for the DC-tests (described in section 4.2.3) and the deposition of the dielectric, all the fabrication steps up to the dicing were performed in a clean room environment. The deposition of the dielectric with atomic layer deposition (ALD) was done in a *grey room*.

4.1 Design of Resonators with and without Top Ground

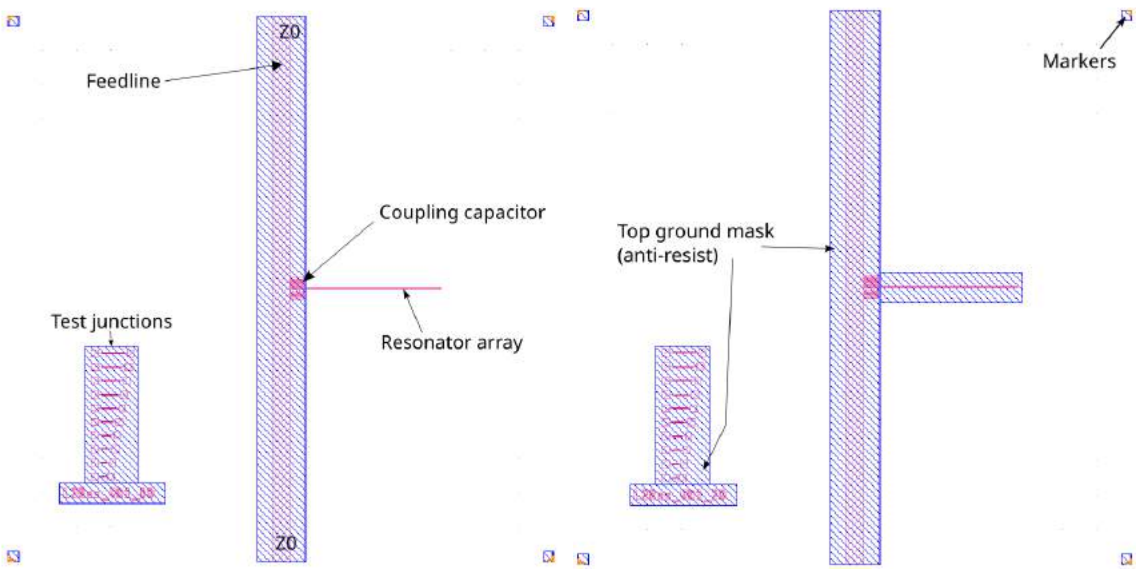

Figure 4.1: GDS implementation of the two resonator types. The feedline, finger capacitor and the Josephson junction array ($\lambda/2$-resonator), as well as the test junctions to the left, are visible in red. The blue areas mark, where the metallic ground will not be deposited (negative resist). Therefore the mask on the left is for the resonators with top ground, the right mask for the resonators without top ground.

The idea to build resonators with the same properties of the junction array as the built amplifiers is adapted from L. Planat [38]. It allows for a precise measurement of dielectric losses. In this work we take an equivalent design of the resonators used in [38], with a few changes: The resonator array consists of single Josephson junctions, instead of superconducting quantum interference devices (SQUID) consisting of 2 junctions in a loop. Additionally, a geometry without the close metallic ground on top of the junction array, called *top ground*, is built and measured. In doing so, the influence of the top ground and therefore the dielectric it encloses with the array can be isolated in a way. This helps to investigate the sources of the losses that we aim to reduce. As mentioned earlier, the purpose of the top ground in a TWPA is to match the impedance of the transmission line to 50 Ω. This is done by increasing the capacitance to ground C_g of the junction array. The C_g without top ground, would come from the ground which is evaporated on the bottom of the wafer. The top ground which is separated from the array by a dielectric with a thickness of only a few 10 nm, leads to an increase of C_g (on the order of a few hundred). Therefore in this case it will outweigh the effect of the capacitance to the far away ground. The resonator circuit design is shown in Fig. (3.6). It consists of a feedline which is coupled to the Josephson junction array (functioning as a $\lambda/2$ resonator) by a capacitor. From a transmission measurement of the resonances the quality factors can be extracted. This allows for a direct estimation of the dielectric loss (Eq. 2.26).

The feedline will be connected to the outside environment. It is a transmission line in a coplanar waveguide (CPW) geometry [37]. It is 8 mm long and 238 µm wide and is created in the same fabrication step as the coupling capacitor and the Josephson junction array, as will be explained in detail later. To achieve the desired high coupling strength, a interdigitated capacitor is used. It consists of 11 fingers with length 190 µm and a width of 20 µm. They are separated by 10 µm. The value of the capacitance will be estimated in a chapter 6.

The junction array is connected to the coupling capacitor with a small connecting pad. The array consists of 600 Josephson junctions. To match the area of the SQUIDs used in [38], they are designed to be 10.5 µm high and 0.8 µm wide. Each junction is connected to the next by a wire of height 0.35 µm and a length of 2.447 µm (about 3 times the junction width). The whole array then has a length of ≈ 2 mm. The design files were created by adapting a Python script, which uses a module of the *gdstk* library. The design files in *.gds* can be converted and then read by the machine performing the lithography. They are shown in Fig. 4.1. The red areas show where the feedline, capacitor and junction array will be placed on the chip. The junction arrays to the bottom left are used for the DC tests, for estimation of the Josephson critical current, and to check the quality of the junctions. For the devices without top ground on the array a distance of 80 µm is left at the end of the resonator array. To the sides, the area is 440 µm wide. This leaves a gap of about 215 µm to both sides of the junctions. Note that the blue areas mark, where the top ground will not be placed (a negative resist is used). This will become clear in the following sections. As the two geometries are fabricated on the same wafer the process is exactly identical except for the evaporation of the top ground on the junction array.

4.2 Fabrication

4.2.1 Preparation of the Wafer

The structure is written on an intrinsic (pure), one side polished silicon wafer with circular shape and a segment cut off to leave one straight edge[1]. It has a 2 inch diameter and a thickness of (275 ± 25) µm. To start with the preparation of the wafer for the writing of the structures, gold is deposited on the unpolished (referred to as bottom) side of the wafer. It acts as a metallic ground and allows for a good thermal contact of the chip to the sample holder later on.

Electron beam lithography is used to write the structures on the wafer. The e-beam writer

[1] This helps to keep track of the orientation (especially important if the substrate has orientation dependent properties) and makes the handling with some tweezers easier.

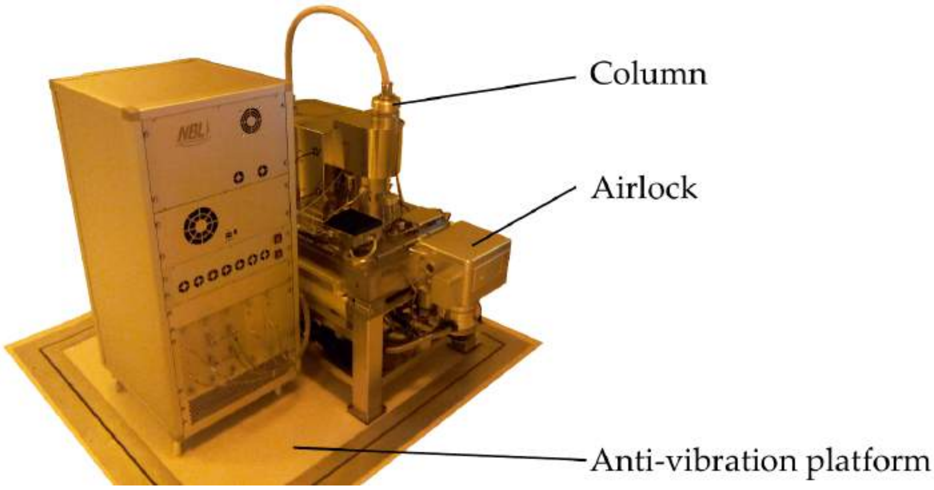

Figure 4.2: Picture of the e-beam writer. It is placed on an anti-vibration platform to be decoupled from vibrations of the clean room building. From [53]

used at the Nanofab clean room at the *Néel Institut* is the model *n*B5 from *NANOBEAM LTD* (see Fig. 4.2). To prepare the wafer for the writing of our resonator structures and to enable the electron nano beam to reach its precision, markers have to be written on the wafer. The mask is a 4x4 grid (16 chips), with each square 8 mm wide. The wafer has global dicing marks that point at where it is later cut to separate the several chips. It also has local marks which will be used for the focusing of the electron beam. The electron nano beam operates by moving the chuck, where the wafer is loaded upon, in steps of 250 µm. For each of these positions the beam can then be more precisely redirected by magnetic coils. To reach the desired precision, the beam has to account for the tilt of the wafer in the machine. For the writing of the first marks the focusing is done manually. This is the only time where dust on the wafer can come to good use, as the beam can be focused until the features of the dust particles are distinctly visible. Later on in the process the beam focuses automatically and locally for each chip by using the local marks of known size. This leads to higher precision and allows for the fabrication of small structures like the Josephson junctions.

To write a structure on a wafer using electron beam lithography, the steps are usually the following.

- **Spin coating:** By spinning the wafer, a fluid (called resist) put on top will spread uniformly. The wafer is then heated (baked) on a heating plate to solidify the resist.
- **Writing:** The resist coated wafer is loaded into the e-beam writer. The resist is exposed to the e-beam at the spots where the structure should be located (with negative resist it is the other way around → see top ground, Sec. 4.2.5). This exposure changes the solubility of the resist.
- **Development:** The wafer is placed in a chemical solution. The exposed resist is dissolved and removed from the layer on top of the wafer.
- **Metal deposition:** A metal is evaporated onto the wafer. Where the resist was removed during the development step, the metal is deposited directly onto the wafer.
- **Lift-off:** To finish the lithography step with only the metal evaporated directly on the wafer, the rest has to be removed. The remaining resist which was not exposed to the e-beam, is dissolved in a chemical solution. This also removes the metal deposited on top of it, hence leaving just the structure on the wafer.

As part of the wafer preparation, it was spin-coated with polymethyl methacrylate (PMMA) 3% and the markers as well as the 4x4 chip mask was written on it. The development is done by placing the wafer in a beaker of a mix of methyl isobutyl ketone and isopropanol (MIBK-IPA) (1:3) for 60 s and then in another beaker of IPA for 30 s. Directly afterwards, the wafer is blow dried using Nitrogen gas (N_2). To reduce the contamination on the wafer, it is important to clean the beakers before using them. The standard procedure for every beaker is to clean it with soap, rinse three times with deionized (DI) water, N_2 blow dry it and then rinse it with the solution which it is then filled with.

For the deposition of the metal, a *PLASSYS©MEB550S* electron-beam physical vapor deposition machine is used. The wafer is loaded into the upper vacuum chamber, which is then pumped. When it reaches a pressure of 1.3×10^{-4} mbar, the valve to the lower vacuum chamber (with a better vacuum), where different metal crucibles are located, is opened. After choosing the crucible with the metal of choice, an electron beam can be focused manually on it. This makes the metal evaporate towards the wafer. There is, however, still a shutter in between the wafer and the evaporating metal. It enables us to set the rate of deposition to ≈ 0.1 nm/s. Thickness is measured through a resonant crystal next to the wafer which lowers its frequency when metal is deposited on it. When the rate is constant the shutter is opened and the evaporation onto the wafer begins. At the start of the process the total pressure in the chambers is at around 9.3×10^{-6} mbar. Note that for titanium (Ti) the crucible will continue to emit atoms for a bit even after turning off the electron beam. For the markers we first deposit 5 nm of Ti and then 50 nm of gold (Au) on the top side of the wafer (with the deposited resist). The Ti helps the Au stick to the wafer. After closing the valve between the chambers, the upper chamber is then vented to be able to open the loadlock. The wafer is turned around and the process is repeated. On the unpolished side of the wafer 10 nm of Ti and 200 nm of Au are deposited. This layer will act as a metallic ground for our structures and ensures a good thermal and electric contact of the chip to the sample holder.[2]

For the metal lift-off, the wafer is placed in a bath of N-Nethylpyrrolidone (NMP) on a heat plate at $80°C$ for more than 5 hours. This dissolves all the remaining resist. Making use of a pipette, the metal on this resist can be flushed away to help to lift off the metal on the top side of our wafer which we do not want. Only the markers (and of course the metal on the bottom of the wafer, which was evaporated directly onto it) remain. The wafer is then rinsed with a shower of acetone, ethanol and IPA (in this order). It is placed on a cleanroom paper and dried with a nitrogen gun.

As this concludes the preparation of the wafer it is now ready for the writing of the structures. Let us review the technique that is used for the fabrication of long Josephson junction arrays.

4.2.2 Josephson Array Fabrication

To fabricate Josephson junction arrays we make use of the *bridge free fabrication (BFF)* technique [44][53]. It avoids the use of a suspended bridge like the *Niemeyer-Dolan* technique [54] and therefore allows for a stable construction of long arrays of junctions. The junctions consist of aluminum, closely separated by an oxide layer.

The different steps are shown in Fig. 4.3. The idea is to create undercuts with a two layer resist, to then evaporate the aluminum from opposite angles, performing an oxidation step in between.

[2]For another batch of wafers, the evaporation steps for the markers and the metal ground on the bottom of the wafer were reversed for practical purposes. There are indications that this led to more contamination on the (more important) polished side of the wafer, since there was no Au layer to shield it when placing it on this side in the deposition machine.

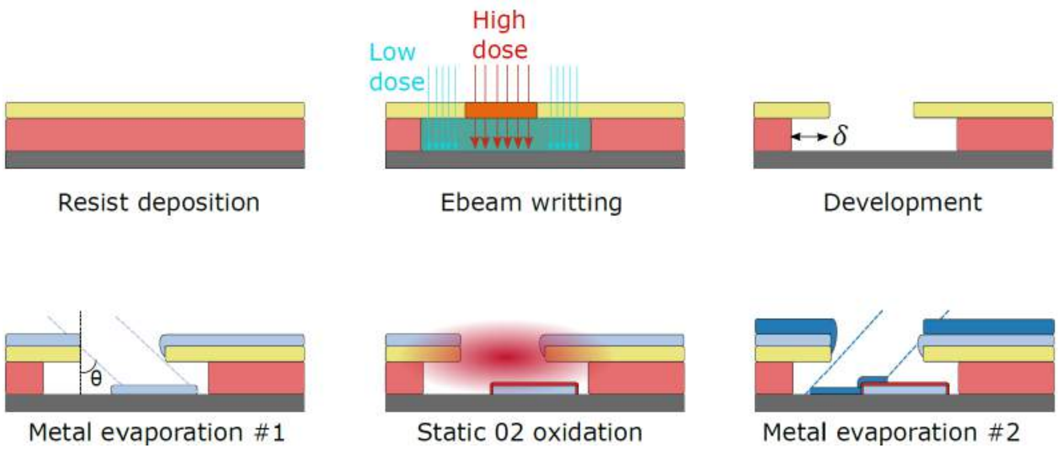

Figure 4.3: The fabrication steps for the BFF technique used to produce the Josephson junction arrays. Two layers of resist are exposed to varying doses of the e-beam writer. The created undercuts allow for double angle evaporation with an oxidation step in between to create the Josephson junctions. [38]

To make an undercut possible, two different types of resist are spin-coated on the wafer (grey in Fig. 4.3, not to scale) on top of each other. The bottom one (red in Fig. 4.3) is less persistent to the electron beam than the top one. If at a spot, the wafer is exposed to a low dose during the writing, this leads to the bottom layer dissolving during development, while the top layer is left intact. However, if a spot is exposed to a high dose, the structure of both layers is impaired and they will be removed during development. The undercut now makes it possible to deposit two layers of aluminum with an offset, by evaporating it from opposite angles. The first layer of aluminum is evaporated with an angle θ. Then oxygen is injected into the metal deposition chamber, making the oxidation *in-situ*. This should allow for a good homogeneity in the thickness of the aluminum oxide layer. This is important, since the thickness of the tunnel barrier determines the critical current and therefore the inductance of the junctions[3]. For similar parameters used for the oxidation process the tunnel barriers have a reported value of roughly $\sim 1\,\mathrm{nm}$ [53]. After the oxidation is done, a second layer is deposited with an angle $-\theta$. The thickness of this layer is more than two times higher than that of the first layer to ensure contact on the step from the first oxidized layer to the substrate. The junction is created. Its dimensions correspond to the overlap between the first and second aluminum layer.

The connecting wires between the junctions are done using asymmetric undercuts. This leads to the deposition of only one layer of aluminum on the wafer, since the metal evaporated from the other angle, just sticks to the resist. In Fig. 4.4 an example junction is shown. It does not exactly correspond to the design used in this work, but illustrates the technique.

A patch of the array pattern that is used to determine which areas are exposed by the e-beam with which dose is shown in Fig. 4.5 a). By building the resist layers in this way, the evaporation of the whole array with the junctions and wires, can be performed during this one fabrication step. The resulting layer structure is shown in Fig. 4.5 b). An image taken of the array under an optical microscope shows the same part of the resulting array (see Fig. 4.5 c). The evaporation of the feedline and the capacitor is actually also done during the same evaporation. The evaporation at different angles and the oxidation should however not have a big impact on the behaviour of the larger structures.

[3]The inductance scales exponentially with the barrier thickness (at this length scale), which has been shown to be 3 % homogeneous in the process used. [53]

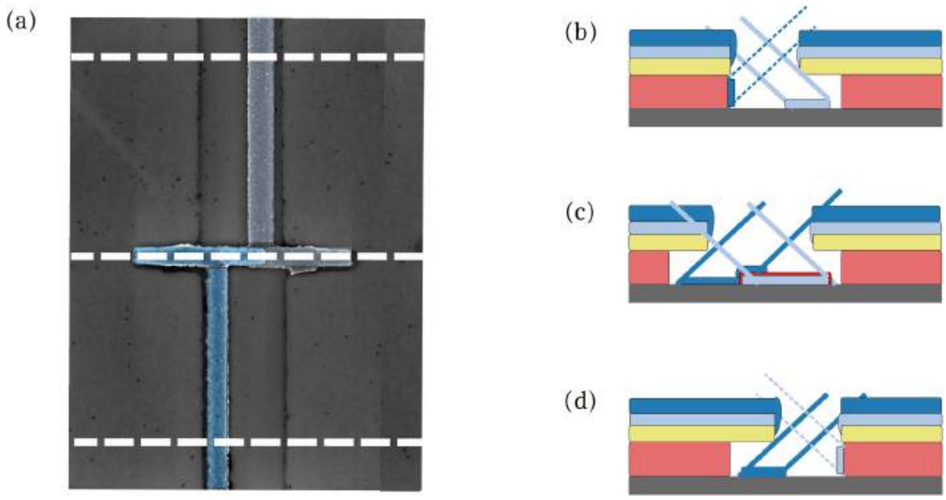

Figure 4.4: (a) A picture taken with a scanning electron microscope (SEM) showing a single junction and its connecting wires. (b-d) Asymmetric and symmetric undercuts lead to overlaps in the metallic layers (junctions) and single layers (wires) respectively. [38]

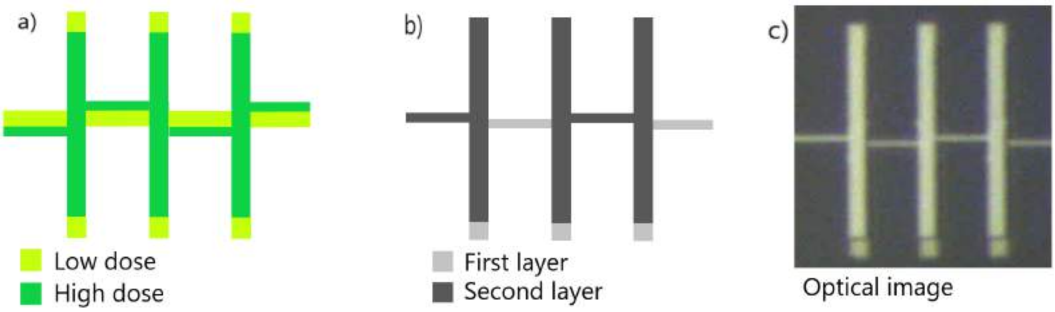

Figure 4.5: (a) Sketch of the dose diagram of a patch of 3 unit cells of the junction array. (b) The resulting junction and wires from double angle evaporation. (c) Optical image of the fabricated Josephson junctions (Taken after top ground lift-off).

For the fabrication of the resonators, the first (more sensitive to the e-nanobeam) layer of resist, had a measured thickness of around (720 ± 10) nm. The second layer was around (235 ± 15) nm thick. These values were measured with an ellipsometer.

After loading the wafer into the e-beam writer the structures are written onto it. Through the writing of all 16 chips the e-beam takes a few breaks to cool down. This prevents damage from overheating. The lithography step took ~ 15 hours and was therefore performed over the weekend. The structures written with low current, such as the Josephson junctions and wires, are written first. Then the large structures of the finger capacitor and the feedline are written with high current (accelerating the writing process).

When the writing is done, the wafer is unloaded from the e-beam writer and taken to development. During the usual steps, the wafer was placed a few seconds less than it was supposed to in the MIBK:IPA (1:3) solution. Looking at it under the microscope it revealed that not all the exposed resist was dissolved around where the interdigitated capacitor is supposed to be placed (see Fig. 4.6).

However, as it turns out, this does not cause deterioration of performance. The reactive ion etching (RIE) done in the next step, helps with removing all of the exposed resist. During RIE, the wafer is exposed to a low power (10 W) oxygen plasma for 15 seconds. After this

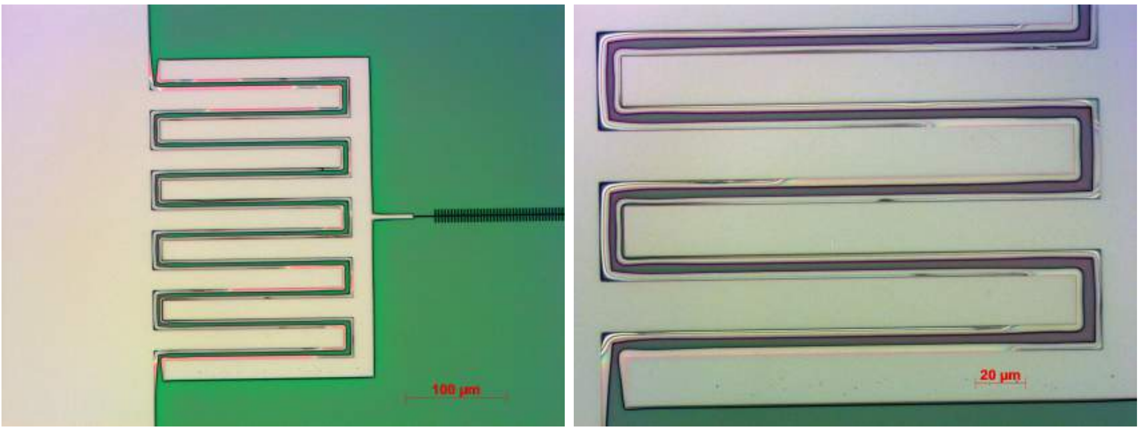

Figure 4.6: Optical images of the resist structure after the lithography step and development.

step, the wafer is ready for evaporation. This is done at another, newer model of the Plassys evaporation system. To allow for the the best possible conditions, the wafer is loaded into the vacuum chamber, which is pumped over night. The vacuum before the first evaporation is below 10^{-7} mbar in both chambers. 20 nm of aluminum are evaporated at an angle of 35°. Then oxygen is injected into the load-lock chamber and the oxidation takes place at 10 mbar for 300 s. After pumping again, 50 nm of aluminum are evaporated at an angle of −35°.

The wafer is put in a bath of NMP on a heat plate @ $80°C$ for about 5 hours. Using a pipette, the detached metal can be sucked and flushed from the wafer. Exposing the beaker to ultrasonic (US) cleaning at 60 % for 60 s helps to dislodge the metal, without damaging the structure of the junctions. The wafer is then rinsed with a shower of acetone, ethanol and IPA and finally dried with an N2 gun. One has to be careful not to blow the wafer away, especially when not holding the gun orthogonal to the wafer surface. The resulting structure is shown in Fig. 4.7.

The recipe for the fabrication of the Josephson junction array is summarized in table 4.1.

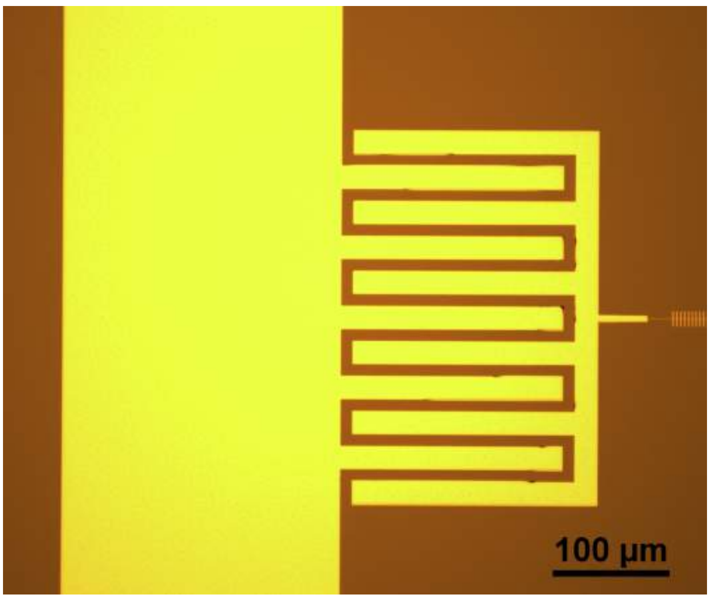

Figure 4.7: Optical image of the feedline, capacitor and the start of the resonator array.

Fabrication step	**Parameters**
Cleaning	RIE: O2, @ 20 W for 120 s
Spin coating	Heat plate: 120 s @ 200°C Resist 1: PMMA/MAA 9 % 3000 rpm, 3000 rpm s^{-1}, 30 s Heat plate: 600 s @ 200°C Resist 2: PMMA 4% 4000 rpm, 4000 rpm s^{-1}, 30 s Heat plate: 300 s @ 180°C
Writing	Feedline/capacitor dose: 10 C m^{-2} (high current) Connecting pad dose: 12 C m^{-2} (high current) Junction/wire dose: 10 C m^{-2} (low current) Undercut dose: 3 C m^{-2} (low current)
Development	MIBK-IPA 1:3 for 60 s IPA 30 s N2 blow dry
Cleaning	RIE: O2, @ 10 W for 15 s
Evaporation	Aluminum 1 : 20 nm @ 0.1 nm s^-1 @ $\theta = -35°$ Oxidation: 300 s @ 10 mbar Aluminum 2 : 50 nm @ 0.1 nm s^{-1} @ $\theta = +35°$
Lift-off	Bath of NMP for 5 hours @ 80°C US for 60 s @ 60 % while holding beaker Rinse: Acetone, Ethanol, IPA + N2 blow dry

Table 4.1: Fabrication recipe for Josephson junction arrays.

4.2.3 DC Tests

The wafer is taken out of the clean room environment to a DC probing station. On each chip of the wafer there are JJ arrays of different lengths (numbers of junctions), so called test junction arrays (see the design in Fig. 4.1). Their purpose is to check, if the fabrication process worked. It is also possible to measure the junctions tunnel resistance R_N at room temperature. This allows to estimate their critical current I_c using the Ambegaokar-Barratoff relation [55]:

$$I_c R_N(T > T_c) = \frac{\pi \Delta_{Al}}{2e}, \tag{4.1}$$

where Δ_{Al} is the superconducting aluminum gap. The value taken for the estimation here is $\frac{\Delta_{Al}}{e} = 210\,\mu\text{V}$. The current sent through the junctions is increased at the DC probing station in steps for several values, while the voltage is measured. The resistance R_N is estimated from the slope of these measurements for the different test array lengths. This allows us to determine the room temperature resistance per junction. By using arrays of different lengths, varying from 10 to 100 junctions, one can also account for the offset caused by the resistance of the probing station.

The test junction arrays were all functional. There was no open or short circuited junction

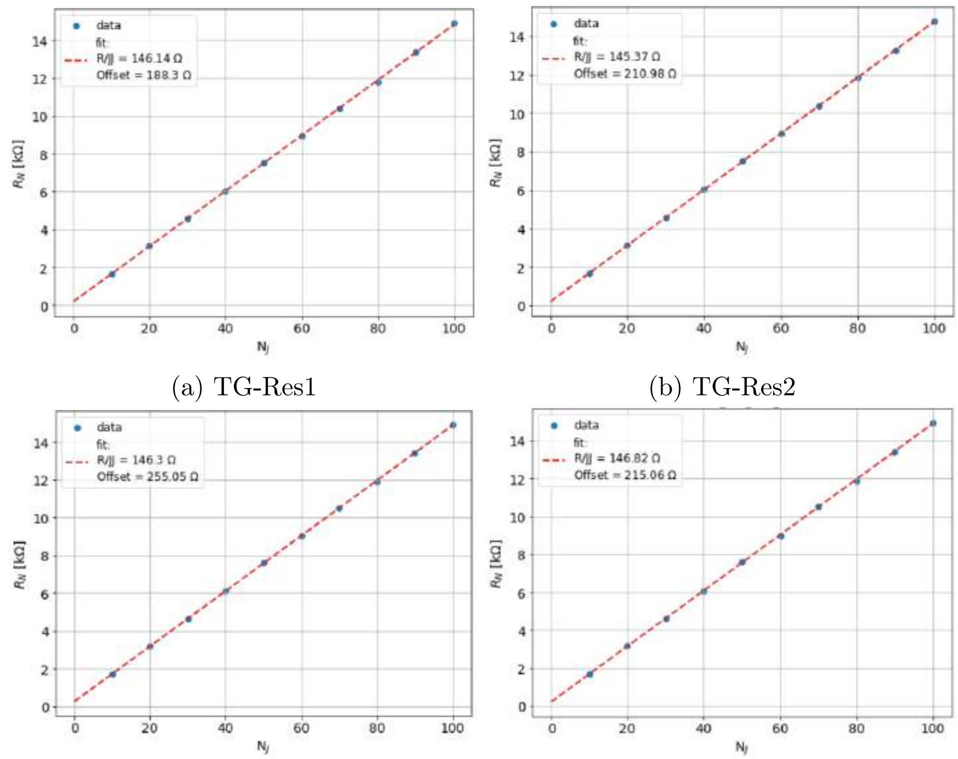

(a) TG-Res1 (b) TG-Res2

(c) Res3 (d) Res4

Figure 4.8: DC test results for the resonators, which are later measured in the experiment.

in any of the test arrays. By using Eq. 4.1, the average critical current evaluates to $I_c = (2.25 \pm 0.02)\,\mu\mathrm{A}$ for the 16 chips measured. With Eq. 3.6 we can estimate the Josephson inductance and get an average value of $L_J = (146.12 \pm 1.13)\mathrm{pH}$. The measured resistance against length is shown in Fig. 4.8 for the devices, later characterized in the cryostat. From previous studies, it is known that L_J will take a new value after heating the junctions in the following atomic layer deposition (ALD) process which is used for the deposition of the dielectric (see Sec. 4.2.4). This is known from performing DC tests after ALD [38], which we skip for our purposes. With another additional factor that accounts for the change in inductance, when going to low temperatures, we can estimate L_J at 20 mK to be

$$L_{J,20\mathrm{mK}} \approx \alpha_{\mathrm{ALD}}\, \alpha_B\, L_J = 161.46\,\mathrm{pH} \tag{4.2}$$

with factors $\alpha_{\mathrm{ALD}} = 0.85$ and $\alpha_B = 1.3$. Taking values from [38] and [53] we can estimate the uncertainty of $L_{J,20\mathrm{mK}}$ at around 5 to 10 %.

Another important purpose of the DC tests is to determine how far away the top ground has to be separated from the array by a dielectric to impedance match the array to $Z_0 = 50\,\Omega$. With $C_g = L_{J,20\mathrm{mK}}/Z_0^2 \approx 64.58\,\mathrm{fF}$ and by modeling C_g as a parallel plate capacitor (Eq. 3.27), we find for the Al_2O_3 thickness $t_d \approx 12.44\,\mathrm{nm}$.

4.2.4 Dielectric Deposition

Atomic layer deposition (ALD) was used to deposit the alumina (Al_2O_3) on top of the resonator array. This technique allows for deposition of single atomic layers of alumina with a precision of around 1Å. The Josephson junction array will be fully covered by the dielectric. This will allow for the deposition of the close metallic ground on top of the resonator. When the process is started, there is an existing native layer of oxide on the aluminum. The ALD

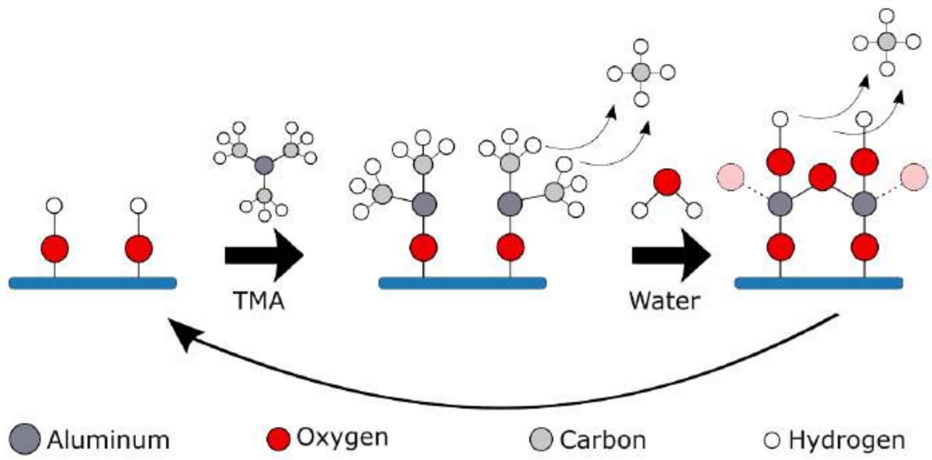

Figure 4.9: The atomic layer deposition (ALD) [38]

.

process goes through several cycles, building the dielectric layer by layer. One cycle is illustrated in Fig. 4.9. First, trimethylaluminum (TMA) is injected into the chamber. It reacts with the oxygen atoms to form bonds to the aluminum. In the next step, a pulse of water is injected to wash away the methyl groups and an oxide layer remains. As estimated before, a thickness of around 12 nm is needed for impedance matching of the array in the geometry with a top ground directly above the array. Each cycle grows around 1 Å of alumina. With $N_c = 220$ cycles the resulting thickness is around 220 Å$\approx$ 22 nm. During the process the deposition chamber is at a temperature of 150°C and a pressure of 2.27×10^{-1} mbar. One cycle consists of a 15 ms pulse of TMA, a 10 s wait and a 15 ms pulse of water followed by another 10 s wait. The wafer was in the deposition chamber for about 90 min. The recipe is summarized in table 4.2.

Step	**Parameters**
Chamber preparation	Temperature: 150°C Pressure: 0.227 mbar
ALD	Number of cycles: 220 TMA pulse: 15 ms Wait: 10 s Water pulse: 15 ms Wait: 10 s

Table 4.2: Recipe for the dielectric deposition with ALD.

4.2.5 Top Ground Deposition

The second and last lithography step is done to deposit the top ground on our structure. For half the resonators, we want to deposit it also directly on top of the resonator array. As the metallic layer we choose 400 nm of copper. When the thickness of the metal is below or comparable to its skin depth, increasing its thickness decreases the conductor losses. In the past, when the thickness was too big there had been issues with the dicing [38]. The top ground should be on the sides of the feed line. This gives a nearly coplanar waveguide geometry since the top ground is merely a few nm higher than the feed line, separated by the dielectric. To reduce the writing area and therefore the writing time, a negative resist is used. This allows to expose only the parts of the resist to the e-beam where we do not want the metal to be directly evaporated onto the structure. In the optimal case the resist should be a few times thicker than the layer of metal that is deposited on it. To get close to this, a resist called *ARN 7700-18* was used. The rotational speed of the spin coater is set to 750 rpm for 90 s with an acceleration of 500 rpm/s. The wafer is baked on the heating plate for 90 s at 85 $°C$. The measured resist thickness was (905 ± 25) nm, which is a bit more than twice the copper we want to deposit. The wafer is loaded in the e-beam writer and the lithography is performed. Thanks to the use of the negative resist lithography only takes ~ 3 hours. Afterwards the wafer is baked again on the heating plate for 2 min at 100 °C. For the development the wafer was put in *AR-300-46* for 2 min 30 s. Then in deionized (DI) water for another 45 s+45 s in two different beakers to clean the wafer. As usual the wafer is dried with the nitrogen gun. DI water may easily leave stains and takes some time to fully evaporate off the wafer.

Reactive ion etching (RIE) at 10 W for 15 s is performed, before loading the wafer for evaporation. The new Plassys evaporation system is used (same as for the aluminum evaporation). A 10 nm layer of titanium is evaporated at around 0.05 nm/s. Then the copper layer of 400 nm is evaporated at a rate of around 0.5 nm/s.

The top ground lift-off was done by leaving it in *AR 300-76* at 80 °C over night. It lifts off nicely by shaking the beaker and using ultrasound at 20% intensity for 2 times 15 s. Afterwards, the wafer is rinsed with acetone, ethanol and IPA for about 10 s each. By switching fast between the steps it is ensured that the wafer does not dry during the rinsing. Then it is dried with nitrogen gas. The recipe is summarized in table 4.3. The final structures (with and without top ground over the resonator array) are shown in Fig. 4.10.

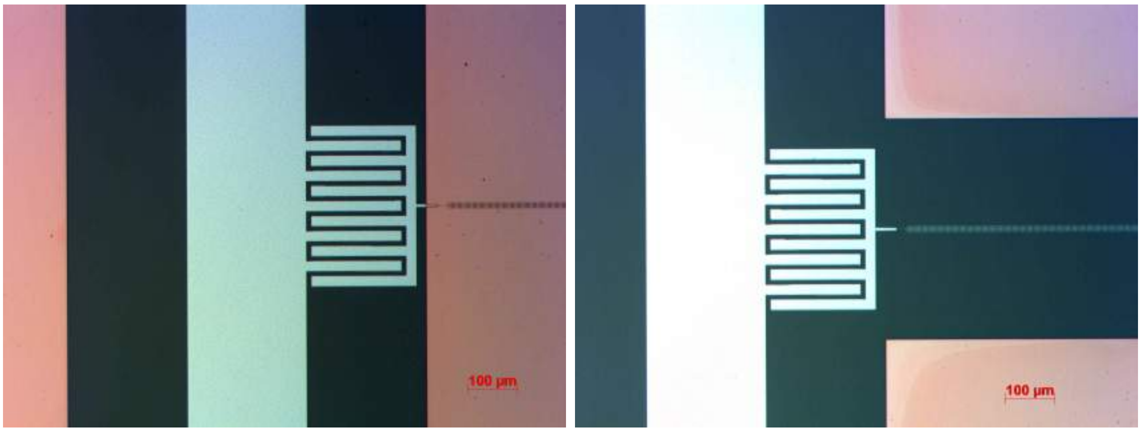

Figure 4.10: Optical images of the resonators after top ground lift-off. Even with the evaporated copper top ground, the structure of the Josephson junction array can be seen optically on the left picture.

4.2.6 Dicing and Wire Bonding

In the dicing procedure the wafer is cut into the 16 square chips of side length 8 mm with a precision diamond saw. To protect the structures, a resist is deposited beforehand. We use *AZ 4562* and spin coat it with 1000 rpm, 100 rpm/s over 40 s. Then it is put to dry on a heating plate for 5 min at 95 °C. The dicing was performed at *MINATEC - Grenoble INP*. After dicing, each chip is cleaned separately by putting it for 60 s in acetone, 30 s in ethanol and 30 s in IPA. Then it is dried with nitrogen gas.

Fabrication step	Parameters
Spin coating	Resist: ARN 7700-18, 750 rpm, 500 rpm s^{-1}, 90 s Heat plate: 90 s @ 85°C
Writing	Negative resist, high current Heat plate: 120 s @ 100°C
Development	AR-300-46 for 150 s DI water 45 s + 45 s N2 blow dry
Cleaning	RIE: O2, @ 10 W for 15 s
Evaporation	Titanium: 10 nm @ 0.05 nm s^-1 Copper: 400 nm @ 0.5 nm s^{-1}
Lift-off	Bath of AR 300-76 for 2 hours @ 80°C US for 30 s @ 20 % while holding beaker Rinse: Acetone, Ethanol, IPA + N2 blow dry

Table 4.3: Fabrication recipe for the copper top ground.

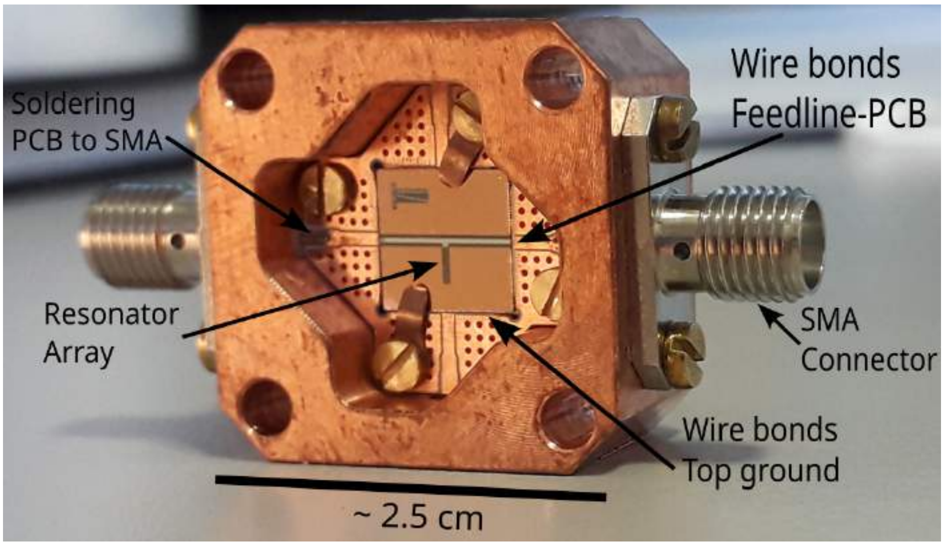

Figure 4.11: Photograph of the device in the sample holder box. The chip is clamped onto the PCB which connects the SMA connectors coming from the cryostat microwave lines to the feedline. Through the thin aluminum wire bonds it is connected to the top ground of the chip.

To be able to measure the samples in the experimental setup, they have to be connected to the measurement apparatus. Since the goal is to measure the transmission, both sides of the feed line have to be connected to the microwave transmission lines of the fridge. This is done in the following steps. The chips is mounted on a printed circuit board (PCB), which itself is placed on a sample holder box made out of copper. The PCB allows to ground the bottom and top of the chip, while providing a connection between the feed line to the subminiature A (SMA) connectors of the setup. It is clipped and screwed to the sample holder for a good thermal and electric contact and soldered to the SMA connectors of the sample holder. A wire bonding machine is used to connect the chip to the PCB. It uses thin aluminum wires and stitches them to the chip and the PCB using ultrasonic bonding. Around 3 to 6 wires could be placed to connect each side of the thin feedline with the PCB. The pressure and vibration is enough to pinch through the thin layer of alumina on top of the feedline[4][38]. The top ground is connected with wires all around, to ensure good grounding. One of the final devices, ready to be installed into the cryostat, is shown in Fig. 4.11.

[4] We used the standard settings recommended by the bonding machine personnel.

Chapter 5

Experimental Setup

5.1 Dilution Refrigerator

The Josephson junctions in the resonator arrays, consist of aluminum. To use their properties, it is necessary to operate them below the superconducting transition temperature of aluminum $T_c \approx 1.2\,\mathrm{K}$ [56]. To be able to precisely measure the device under test (DUT), it is also required to reduce thermal noise [57]. The mean number of thermal photons is given by the *Bose-Einstein* distribution

$$n(\omega, T) = \frac{1}{e^{\frac{\hbar\omega}{k_B T}} - 1}\,. \tag{5.1}$$

For a frequency of 2 GHz, the mean thermal photon number is already below $n \sim 10^{-2}$ at a temperature of 20 mK. As it gets lower for higher frequencies, the thermal noise can rightfully be neglected at this temperature in the frequency range of 2 to 12 GHz, that the measurements are performed at. To reach such low temperatures, the cryostat used is a dilution refrigerator.

It uses a mixture of helium-3 and helium-4 and their enthalpy of mixing to achieve cooling [58][59]. The opened up dilution fridge with its five temperature stages is shown in Fig. 5.1. The coldest 20 mK stage is on top (inverted dilution fridge).

The temperature at different points (e.g. next to the cold plate) is being logged during the measurements. The DUT are screwed to a copper mount for good thermal contact. The box, where the chip with the resonator is housed, is itself out of copper. They should therefore reach a temperature close to the base temperature as well. The four samples are placed next and opposite to each other on the same copper mount.

5.2 Measurement Lines and VNA

The two ports of a vector network analyzer (VNA), operating at room temperature, are connected with coaxial cables to the DUT. To rid the input signal of the room temperature noise of the VNA, it is attenuated several times on its way. The input line attenuation is shown in Fig. 5.2. It was obtained from another measurement and gives the attenuation between the VNA and the DUT for the given frequency. On the way from the DUT to the VNA, the signal is amplified again, using a HEMT amplifier operating at the 4 K stage.

For the first measurements, an *Anritsu* VNA (model MS46522B) was used. Later on, all the measurements were done with the ZNL14 by *Rohde Schwarz*.

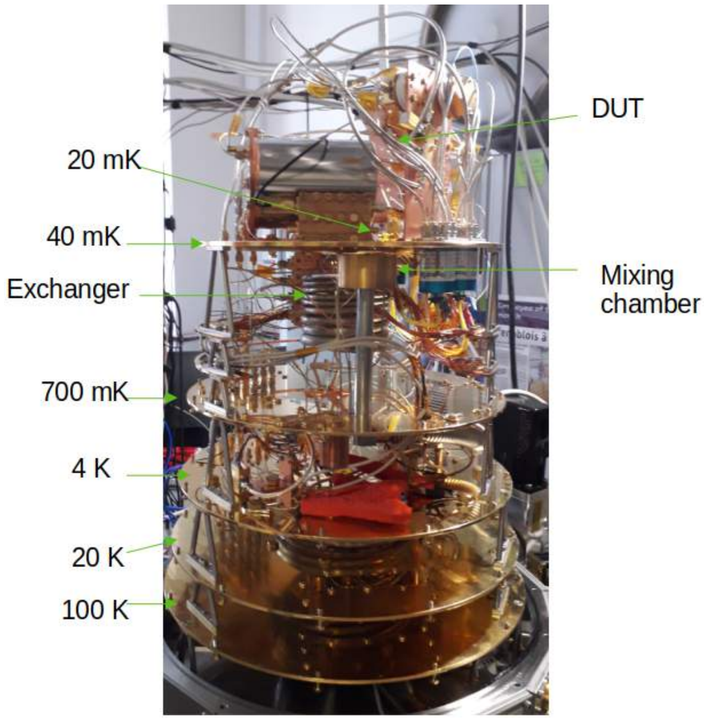

Figure 5.1: Photograph of the dilution refrigerator showing the different temperature stages. The device we want to measure is placed and screwed on a copper mount that is connected to the cold plate.

A cryogenic coaxial switch makes it possible to change back and forth between the different devices. After switching, the temperature at the temperature sensor at the cold plate goes up for a few minutes, but settles at around 20 mK again soon.

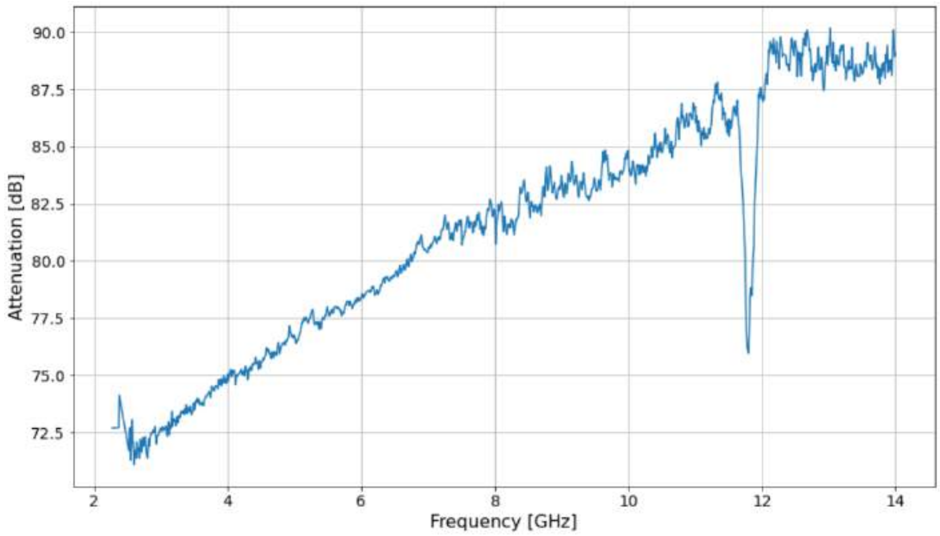

Figure 5.2: Input line attenuation between VNA output and DUT.

Chapter 6

Simulations and Calculations

6.1 ABCD Matrix Simulations

Setting up the resonator circuit using the ABCD matrix method, gave a simple model of the setup and some insight about how the system would behave with a change of the different parameters. The model was built according to Fig. 3.6, implementing losses by adding a resistance R_{ESR} at each capacitance to ground C_g, according to

$$R_{\mathrm{ESR}} = \frac{\tan(\delta)}{2\pi f\, C_g} \tag{6.1}$$

with frequency f and $\tan(\delta)$ defined in (2.24).

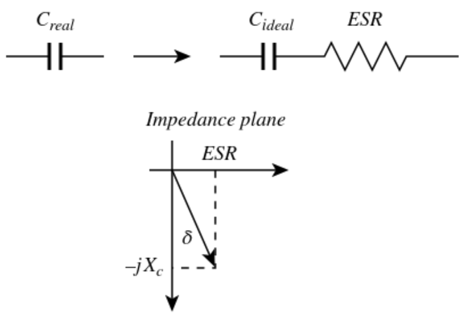

Figure 6.1: The equivalent series resistance (ESR): A real capacitor is modeled as a perfect capacitor in series with a resistance. [60]

At the end of the resonator, the open is modeled by connecting it with a very high resistance to the ground ($\sim 10^{13}\,\Omega$).

As parameters, we use $C_{\mathrm{in}} = 1.46 \times 10^{-13}\,\mathrm{fF}$ (close to what it is estimated to be in Sec. 6.2) and $\tan(\delta) = 5 \times 10^{-3}$. The resulting transmission, as the parameter S_{21}, is shown in Fig. 6.2.

By fitting a Lorentzian function 7.1 to the resonances (see chap. 7, Eq. 7.1), the quality factors can be extracted just like it is later done using the data from the actual measurements. The results of the fits for the internal quality factor Q_i and external quality factor Q_e for the resonances in the considered frequency range are shown in Fig. 6.3.

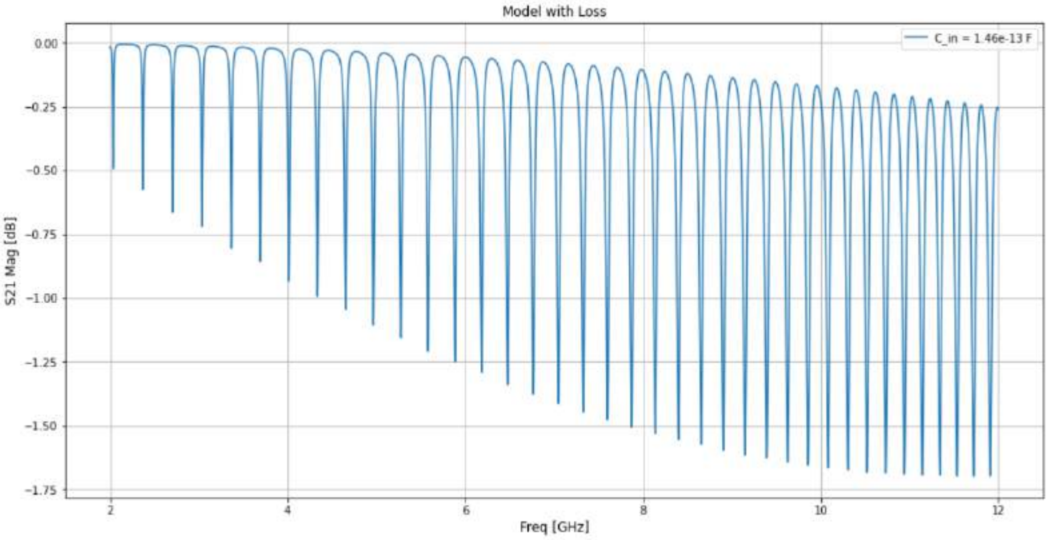

Figure 6.2: The plot shows the transmission, simulated with the ABCD matrix model.

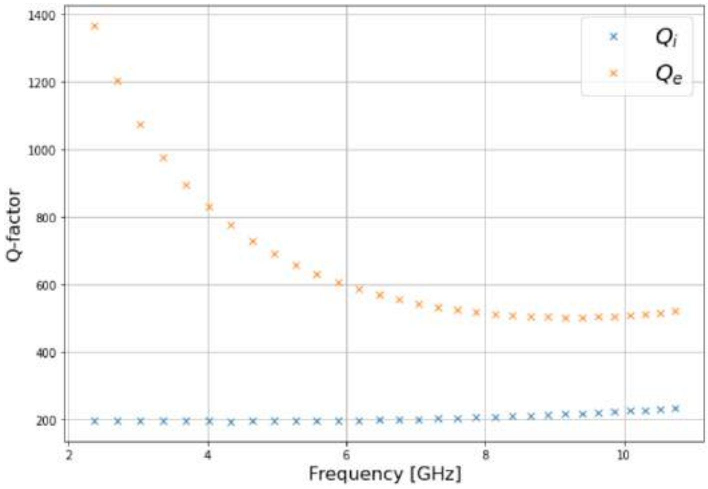

Figure 6.3: The plot shows Q_i and Q_e versus frequency, obtained from the Lorentzian fits of the ABCD matrix model for the resonances in the given frequency range.

6.2 Estimation of the Coupling Capacitance

6.2.1 Coupling Capacitance Obtained by Direct Calculation

Let us estimate the capacitance of the interdigital capacitor (IDC) C_{in}, that was evaporated onto the wafer and couples the feedline to the resonator (see Fig. 3.6 & 4.6), by following the approach of [61]. The idea is to map the structure of the IDC onto a parallel plate capacitor, which we can then evaluate, using the new coordinate system.

The gaps between the fingers are denoted as have a width of G while the N fingers have a width of W. Their length is given by L (see

The metallization ratio is given as

$$\eta = \frac{W}{W+G} = \frac{2W}{\lambda}\,, \tag{6.2}$$

with the spacial wavelength $\lambda = 2(W+G)$.

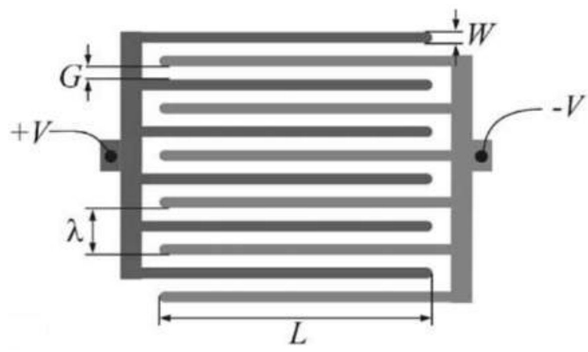

Figure 6.4: The interdigital capacitor (IDC) and its dimensions. [61]

$$C_{\text{total}} = (N-3)\frac{C_I}{2} + 2\frac{C_I C_E}{C_I + C_E} \quad \text{for } N > 3 \tag{6.3}$$

$$C_I = \epsilon_0 L \left(\frac{K(k_{I\infty})}{K(k'_{I\infty})} + (\epsilon_1 - 1)\frac{K(k_{I,1})}{K(k'_{I,1})} + \epsilon_S \frac{K(k_{I\infty})}{K(k'_{I\infty})} \right) \tag{6.4}$$

$$C_E = \epsilon_0 L \left(\frac{K(k_{E\infty})}{K(k'_{E\infty})} + (\epsilon_1 - 1)\frac{K(k_{E,1})}{K(k'_{E,1})} + \epsilon_S \frac{K(k_{E\infty})}{K(k'_{E\infty})} \right) \tag{6.5}$$

with the elliptic integral of the first kind $K(k)$ with modulus k and complementary modulus $k' = \sqrt{1-k^2}$.

$$k_{I\infty} = \sin(\frac{\pi\eta}{2}) \ , \ k_{E\infty} = \frac{2\sqrt{\eta}}{1+\eta} \tag{6.6}$$

The permittivity of the top layer is given by ϵ_1 and that of the substrate by ϵ_S.

If we do not take the finite layer of alumina into account and just consider the IDC on the silicon substrate with a semi-infinite layer of air/vacuum on top of it, the expressions reduce to

$$C_I = \epsilon_0 L(1+\epsilon_S)\frac{K(k_{I\infty})}{K(k'_{I\infty})} \tag{6.7}$$

$$C_E = \epsilon_0 L(1+\epsilon_S)\frac{K(k_{E\infty})}{K(k'_{E\infty})} \tag{6.8}$$

Using the dimensions of our capacitor ($N = 11$, $L = 190\,\mu\text{m}$, $W = 20\,\mu\text{m}$, $G = 10\,\mu\text{m}$) and a relative permittivity for silicon of $\epsilon_S = 11.9$, by plugging everything into (6.3), we find an estimate of the total capacitance of $C_{\text{total}} = 148.89\,\text{fF}$.

With alumina layer: For a more precise estimate, one can think about also considering the thin layer of alumina on top of the capacitor. Its thickness is denoted by h, then we can introduce a parameter

$$r = \frac{h}{\lambda} \, . \tag{6.9}$$

Through conformal mapping techniques, the interior electrodes capacitance is then mapped onto the capacitance

$$C_{I,\text{new}} = \epsilon_0 \epsilon_r L \frac{K(k_I)}{K(k_I')}\,, \tag{6.10}$$

with $k_I' = \sqrt{1 - k_I^2}$, where k_I is now given as

$$k_I = t_2 \sqrt{\frac{t_4^2 - 1}{t_4^2 - t_2^2}}\,, \tag{6.11}$$

with

$$t_2 = sn(K(k)\eta, k)\,. \tag{6.12}$$

sn denotes the Jacobi elliptic function. $t_4 = 1/k$ with

$$k = \left(\frac{v_2(0,q)}{v_3(0,q)}\right)^2\,, \tag{6.13}$$

where v_2 and v_3 denote the Jacobi theta functions with

$$q = e^{-4\pi r}\,. \tag{6.14}$$

C_E is also expressed as a parallel plate capacitor

$$C_{E,\text{new}} = \epsilon_0 \epsilon_r L \frac{K(k_E)}{K(k_E')} \tag{6.15}$$

with $k_E' = \sqrt{1 - k_E^2}$, where k_E is now given as

$$k_E = \frac{1}{t_3} \sqrt{\frac{t_4^2 - t_3^2}{t_4^2 - 1}}\,, \tag{6.16}$$

with

$$t_3 = \cosh \frac{\pi(1-\eta)}{8r} \tag{6.17}$$

and

$$t_4 = \cosh \frac{\pi(1+\eta)}{8r}\,. \tag{6.18}$$

If this is evaluated with standard methods (Mathematica and scipy implementations of the functions used) for a very thin alumina layer of only $h \approx 22\,\text{nm}$, the term for k (6.13) will give 1 for $q \approx 1$. $K(k)$ for $k = 1$ however, diverges.

To resolve this issue, one can express the ratio of the Jacobi theta functions (6.13) as a continued fraction and perform the calculations in a high precision framework[1]. For our alumina layer thickness, the values for the ratio of the Jacobi elliptic functions in (Eq. 6.10 and 6.15) are around $C_{I,\text{factor}} \approx 1.4582 \times 10^{-3}$ and $C_{E,\text{factor}} \approx 4.3915 \times 10^{-3}$. When plugging these values into (Eq. 6.4 and 6.5) as the ratio in the middle term (for the finite dielectric layer), one ends up with the C_I and C_E, that take the alumina layer into account.

Finally putting this into Eq. 6.3, we end up with $C_{\text{total}} = 149.01\,\text{fF}$. As this is very close to the value estimated without the dielectric, we can conclude that its influence can be neglected.

[1] A decimal accuracy of 5×10^4 was used and the continued fraction was performed over 1.5×10^4 recursions.

L (nH)	C (fF)
5	176
6.7	175
50	171
10	176
From 6.2	149

Table 6.1: Capacitance derived from resonance frequency for different values of L.

6.2.2 Coupling Capactiance Obtained by Simulation via Sonnet Software

Another way of obtaining an estimate for the capacitance of the coupling capacitor, is via the use of 3D EM wave simulations. This can be done with Sonnet software [62].

We replicate the structure in the simulation program, as it is fabricated on the wafer. The dimensions of the feedline, capacitor, copper top ground, the wafer and the gold ground on the bottom are set to the same values. The layout is shown in Fig. 6.5. The thickness of the different layers is given in table 6.2. The metals used have standard values of conductivity. The superconducting Aluminum is set to be lossless. Instead of coupling the finger capacitor to a resonator transmission line, it is connected to a perfect inductor, that is grounded on the other end. The ground is at the side of the box, which limits the simulation. The box has a base area of $8 \times 8\,\mathrm{mm}^2$, like the chip. It is subdivided into a grid of $2\,\mu\mathrm{m}$ on the x-axis (the one orthogonal to the feedline), to be able to correctly simulate its width of $238\,\mu\mathrm{m}$. After testing out different cell sizes of the y-axis, it is chosen to be $10\,\mu\mathrm{m}$. This is enough to precisely represent the structure and speeds up the simulation (by reducing the number of cells by a factor of 5 compared to a $2\,\mu\mathrm{m}$ subdivision of the grid on the y-axis).

The idea is to simulate the transmission between two ports at the ends of the feedline and infer the value of the capacitance from the resonance frequency f_0 of the LC circuit, as

$$C = \frac{1}{4\pi^2 L f_0^2} \,. \tag{6.19}$$

Fig. 6.6 shows the transmission (S_{21}) of the feedline plotted against the frequency for different values of the inductance L. Several resonances are visible in the given frequency range. The resonances above 8 GHz do not change significantly in position or shape, when the inductance is varied[2]. The first resonance however, moves towards lower frequencies when L increases. This resonance can be identified as the one of the resonator consisting of the IDC and the perfect inductor. By using Eq. 6.19 we get the values listed in table 6.1.

Consider the situation with a thin layer of alumina between the plane, which the feedline and the capacitor are in, and the top ground. A 3D-view is shown in Fig. 6.7a. The transmission resulting from this model (see Fig. 6.7c) is almost perfectly the same as the one for the case without the thin dielectric layer (Fig. 6.6c). As in Sec. 6.2, we can conclude that the value of the capacitance itself does not really depend on the thin layer of alumina. Comparing the results, the values obtained by the simulation are around 17% higher than the value from direct calculation. Nevertheless, We should now have a decent estimate of the coupling capacitance used in the resonators.

[2] There is something like a resonance just below 15 GHz, which seems a bit odd. It is not, like the others, a dip in transmission and seems to disappear for higher values of L.

Layer	Thickness
Air/Vacuum	0.5 mm
Copper top ground	400 nm
Alumina	22 nm
Aluminum	70 nm
Silicon	275 µm
Gold	200 nm

Table 6.2: Layer dimensions used for the simulations.

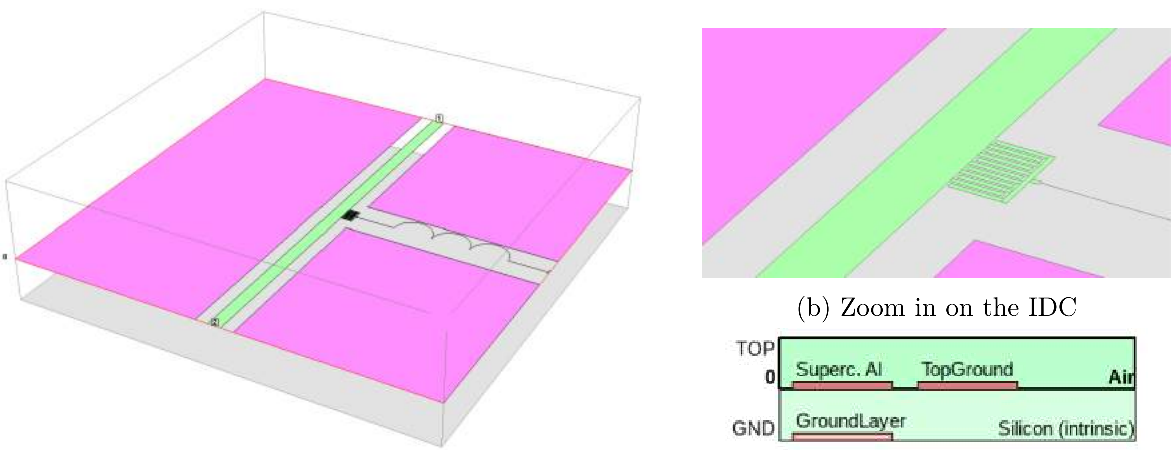

(a) 3D-Overview (b) Zoom in on the IDC (c) Layer structure

Figure 6.5: Overview of the simulated structure.

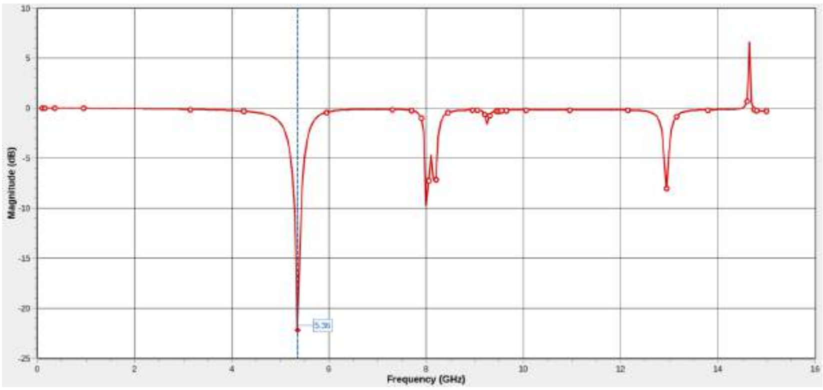

(a) $L = 5\,\mathrm{nH}$

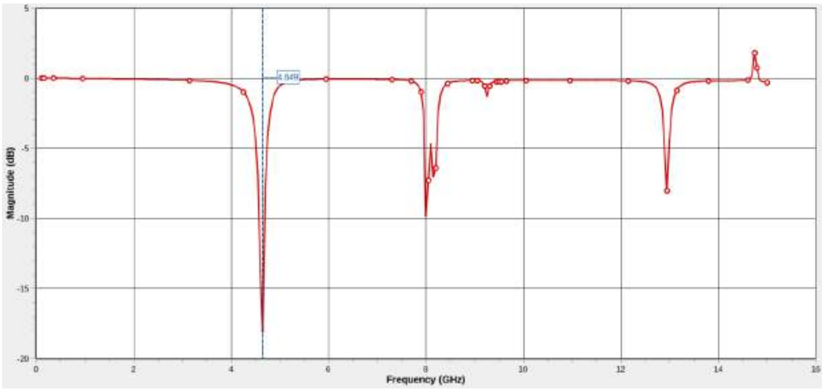

(b) $L = 6.7\,\mathrm{nH}$

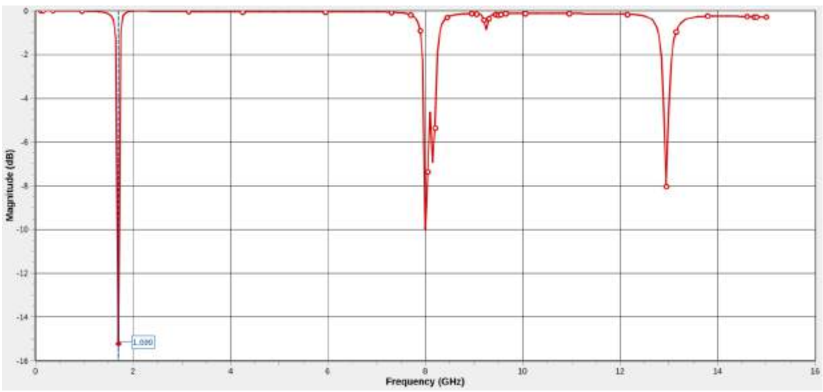

(c) $L = 50\,\mathrm{nH}$

Figure 6.6: Simulations of S21 versus frequency for different values of the inductance L.

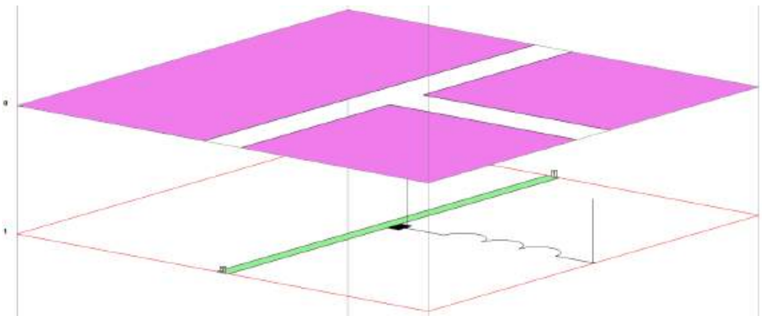

(a) 3D-Overview

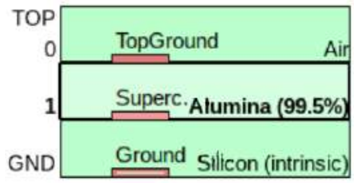

(b) Layer structure

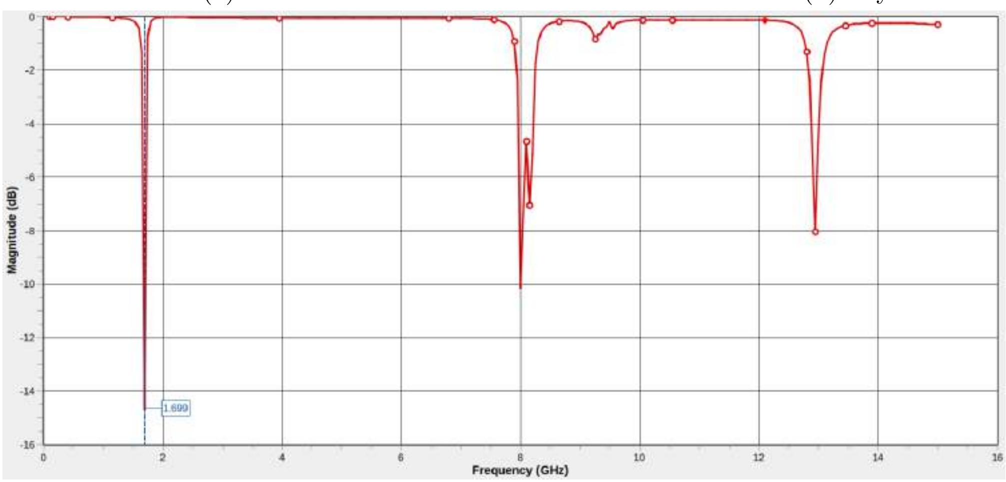

(c) S21 versus frequency for $L = 50\,\mathrm{nH}$

Figure 6.7: The simulated structure with a thin layer of alumina between the aluminum and the copper top ground. The dielectrics and the gold ground below are not shown.

Chapter 7

Data Taking and Processing

7.1 Data Taking

To refer to the different samples, the notation used is *TG-Res1* and *TG-Res2* for the devices with the top ground evaporated above the resonator array. The other two devices measured are called *Res3* and *Res4*.

The data were taken using a vector network analyzer (VNA) connected to the cryostat. A PC was connected to the VNA and was saving and processing the data using *QCoDeS*, a Python-based data acquisition framework. What was measured with the VNA is the S_{21} parameter i. e. in our case the transmission from one side of the feedline to its other end. Since the feedline is coupled to the resonator this allows for a measurement of the resonances. The VNA then takes traces of S_{21} versus the applied microwave frequency. These are performed at a given VNA power. Then we also measure the dependence of the traces with respect to the VNA output power. To do so, sweeps of VNA power are performed for a given frequency and VNA power range. The step size of the power sweep is defined each time. After tesing different settings, the intermediate frequency bandwidth (IFBW) is set to 100 Hz for all the measurements presented in this work.

To be able to cover a larger power range[1], additional attenuators at room temperature can be used. They are added directly after the VNA ouput. We sweep through 40 dB by using a VNA output with the ZNL14 of -40 dBm to 0 dBm. Then two 20 dB attenuators[2] are added and the VNA power sweep is repeated, giving an effective range of up to 80 dB. These two ranges of power will in the following be referred to as high power (no added attenuation) and low power (40 dB of attenuation added). Since the signal is weak at lower powers, one can make use of averaging for a given power value. The VNA sweeps the frequency several times and takes the average values for each frequency bin. This gives much clearer measurements, but also increases measuring times by the factor of the averages taken. For the low power regime, up to 20 averages were used. For TG-Res1 and TG-Res2 the high power range was performed for several resonances in one sweep. Since no averages are needed this is feasible considering measurement times. For the low power regime each resonance is measured separately. In the case of the resonator of sample Res3, the 3 resonances are measured sparately with high precision for high and low power. To get enough data points for performing fits on the resonances, for these data at least 1000 frequency points per GHz were measured. An overview of the parameters is shown in table 7.1.

[1] The ZNL14 VNA can internally cover a range of 40 dB. The MS46522B can cover 30 dB.

[2] Attenuator models: BW-S20-2W263+ and INMET 64671 18AH-20.

Data Set	Device	Freq.	ppGHz	VNA Power	Att.	Avg.
CD1D1	Res3	[2, 15]	500	-10	0	1
CD1D1	Res3	[2, 14]	500	-10	0	1
CD1D2	Res4	[2, 15]	500	-10	0	1
CD1D2	Res4	[2, 14]	500	-10	0	1
CD2D1	TG-Res1	[2, 14]	1000	-10	20	1
CD2D1	TG-Res2	[2, 14]	1000	-10	0	1
CD2D2	Res3	[2,14]	500	0	0	1
CD2D2	Res4	[2,14]	500	-10	20	1
CD2D1	TG-Res1	[4, 7]	1000	[-40, 0]; 0.5	0	1
CD2D1	TG-Res1	[7, 10]	1000	[-40, 0]; 0.5	0	1
CD2D1	TG-Res1	$\sim$4.27	6667	[-30, 0]; 1	40	10
CD2D1	TG-Res1	$\sim$5.02	6667	[-30, 0]; 1	40	10
CD2D1	TG-Res1	$\sim$5.76	6667	[-30, 0]; 1	40	15
CD2D1	TG-Res1	$\sim$6.51	6667	[-30, 0]; 1	40	15
CD2D1	TG-Res1	$\sim$6.86	6667	[-30, 0]; 1	40	15
CD2D1	TG-Res1	$\sim$7.22	6667	[-30, 0]; 1	40	20
CD2D1	TG-Res1	$\sim$7.90	6667	[-30, 0]; 1	40	20
CD2D1	TG-Res1	$\sim$8.60	6667	[-30, 0]; 1	40	20
CD2D1	TG-Res2	[3.5, 7]	1000	[-40, 0]; 0.5	0	1
CD2D3	TG-Res2	$\sim$3.89	6667	[-30, 0]; 1	40	15
CD2D3	TG-Res2	$\sim$5.40	6667	[-30, 0]; 1	40	20
CD2D3	TG-Res2	$\sim$6.14	6667	[-30, 0]; 1	40	20
CD2D3	TG-Res2	$\sim$6.50	6667	[-30, 0]; 1	40	20
CD2D3	TG-Res2	$\sim$6.86	6667	[-30, 0]; 1	40	20
CD2D2	Res4	$\sim$6.62	8333	[-20, -9]; 0.2	0	1
CD2D2	Res4	$\sim$2.71	20000	[-40, -18]; 0.2	0	1
CD2D2	Res4	$\sim$6.63	16667	[-40, -20]; 0.5	0	1
CD2D2	Res4	$\sim$10.07	20000	[-40, -18]; 0.2	0	1
CD2D2	Res4	$\sim$2.71	44445	[-40, 0]; 1	40	15
CD2D2	Res4	$\sim$6.63	40000	[-40, 0]; 1	40	15
CD2D3	Res4	$\sim$10.07	40000	[-20, 0]; 1	40	3
CD2D3	Res4	$\sim$10.07	40000	[-40, -20]; 1	40	15

Table 7.1: Table of parameters for each measurement. IFBW = 100 Hz for all the measurements listed. The frequency is given in units of GHz and the VNA power in dBm, where [a,b]; c denotes the power sweep range from a to b with step size c. The room temperature attenuation (Att.) added directly after the VNA output to reach lower power, is given in dB. The column Avg. denotes the number of averages taken for each trace.

7.2 Procedure for Fits and Extraction of Quality Factors

By fitting a Lorentzian function to the shape of a resonance, both Q_i and Q_e can be extracted. The function which is used to fit the transmission S_{21} around a resonance is derived in [51] and is given by

$$S_{21}(\omega) = \frac{Z_0}{Z_0 + iX_e} \frac{1 + 2iQ_i(\frac{\omega - \omega_0}{\omega_0})}{1 + \frac{Q_i}{Q_e Z_0}(Z_0 + iX_e) + 2iQ_i(\frac{\omega-\omega_0}{\omega_0})} + y_{\text{offset}} \,. \tag{7.1}$$

Since we have the measurements of S_{21} versus frequency, the fit parameters are:

- Q_i is the internal quality factor.
- Q_e is the external quality factor.
- Z_0 is the impedance of the feedline.
- y_{offset} is a parameter to account for the y-axis offset of S_{21}. It is needed because the measured transmission is not calibrated to a transmission of 1 at the resonance.
- X_e is the reactance, which is introduced by considering the feedline as a $\lambda/2$ resonator itself. This is caused by the imperfect bonding of the ends of the feedline to the printed circuit board (PCB). One can include X_e as elements in the resonator circuit (3.6) on both sides of the feedline between the Z_0 from the environment and the coupling capacitance C_{in}. It accounts for asymmetries in the shape of the resonance.
- ω_0 is the angular frequency at resonance. The frequency dependence in Eq. 7.1 appears as a deviation from this resonance frequency.

Note that S_{21} is a complex number. We measure amplitude and phase in the experiment. The phase data was not fitted, but just checked for consistency. For the fits we instead use only the amplitude $|S_{21}|$.

The process of the fits can be automatized to an extent, by initially automatically estimating the resonance peaks and their widths. These can be used as good estimates for the initial values of the fits. It is then possible to fit the data (sometimes consisting of multiple data sets) corresponding to a resonance with the transmission at all the different VNA powers, in one process.

Another additional approach that was pursued is the implementation of a procedure for the fits, which uses two level optimization. The goal is to use functional constraints for parameters like Q_e and Z_0. This allows to implement the assumption, that the external quality factor and the impedance of the feedline do not change with a change in power. This is done by introducing a *meta function* which adds together the deviation (cost) of the fits to the original function we want to fit (Eq. 7.1), as well as from the other constrains we impose. By then optimizing the fit parameters for this meta function, one finds as a result almost constant values for the external quality factor Q_e and the impedance Z_0 (they are still results from the optimization procedure). In other words the fit will estimate the parameters which best represent the data, while also trying to keep Q_e and Z_0 constant across the different VNA powers. This turns out to be especially helpful for data with low power (40 dB of added attenuation) applied (and then especially for the TG-Res1/2 samples), since a good fit to the data with big fluctuations is difficult. Following this approach does not significantly impede the ability of the fits to correctly represent the structure of the measured data. On the contrary, it helps to fit the other parameters more accurately (to more physically meaningful values) as well.

To estimate the quality of the fits it is necessary to have a measure of the uncertainty. As there is no statistics for a single power value of the transmission, one has to estimate the uncertainty directly from the uncertainty of the fit parameters. These uncertainties vary a lot between the parameters, but are low for Q_i, especially for high powers (no attenuation added directly after VNA output). For Q_e the errors were high (of the order of a few hundred), but have been reduced by the two level optimization ($\Delta Q_e < 50$).

If we want to infer the intrinsic losses of the dielectric, we have to look for low power Q_i. Low power in the sense that the input power at the resonator corresponds to the single photon regime.

The average number of photons in the resonator was estimated in ([38][51]) using input-output theory, to be

$$\bar{n} = \frac{2\omega_0/Q_e}{\hbar\omega_0(\omega_0/Q_e + \omega_0/Q_i)^2} P_s \,. \tag{7.2}$$

From a later measurement of the input line attenuation at the DUT (Fig. 5.2) we know the power P_s which enters the resonators. With the quality factors extracted from the fits, we can estimate at which power the average photon number is $\bar{n} < 1$ (let us take for example $\bar{n} \approx 0.1$). We can then take these Q_i to translate it to the corresponding loss tangent. The input power at the resonators estimated with the fits gives values of P_s between $-130\,\mathrm{dBm}$ and $-123\,\mathrm{dBm}$ for the top ground samples. For the sample without top ground P_s is between $-140\,\mathrm{dBm}$ and $-132\,\mathrm{dBm}$ (see table 8.1).

Chapter 8

Experimental Results

8.1 Direct Measurements

8.1.1 First Cooldown

During the first cooldown of the four devices, we checked the transmission of the samples. One of the top ground samples was not working and the wire bonding had to be fixed after warming up.

The measured transmission of Res3 and Res4 are shown in Fig. 8.1. The deep resonances for these devices without the top ground on the resonator array are immediately visible on the plot of the transmission. The transmission is measured using the *Rohde Schwarz* ZNL14 VNA. The (almost identical) results measured with the *Anritsu* MS46522B are shown in the appendix A.3. A power sweep of 40 dB with a 20 dB attenuator after the VNA output was measured. This data was then attempted to be fitted to get an idea of what power ranges have to be measured for each resonance of Res3 and Res4. We could conclude, that we needed a wider power range to measure the whole range of interest.

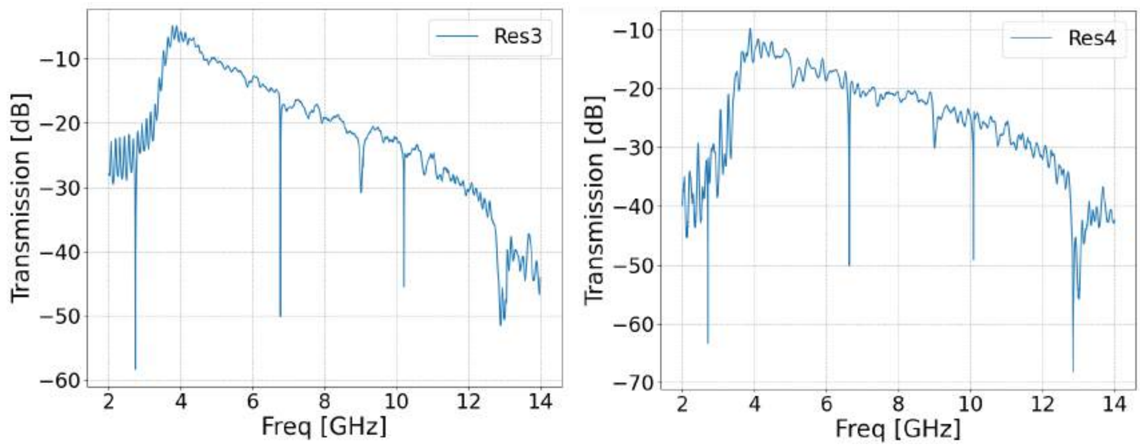

Figure 8.1: The transmission $|S_{21}|$ of Res3 and Res4 measured at a VNA power of -10 dBm.

8.1.2 Second Cooldown

The same devices were cooled down in the second run as in the first one. When looking at the transmission of Res3 and Res4 with 0 dBm however, it appears to be different from what we measured in the first run. Their transmission is shown in Fig. 8.2. The disappearing

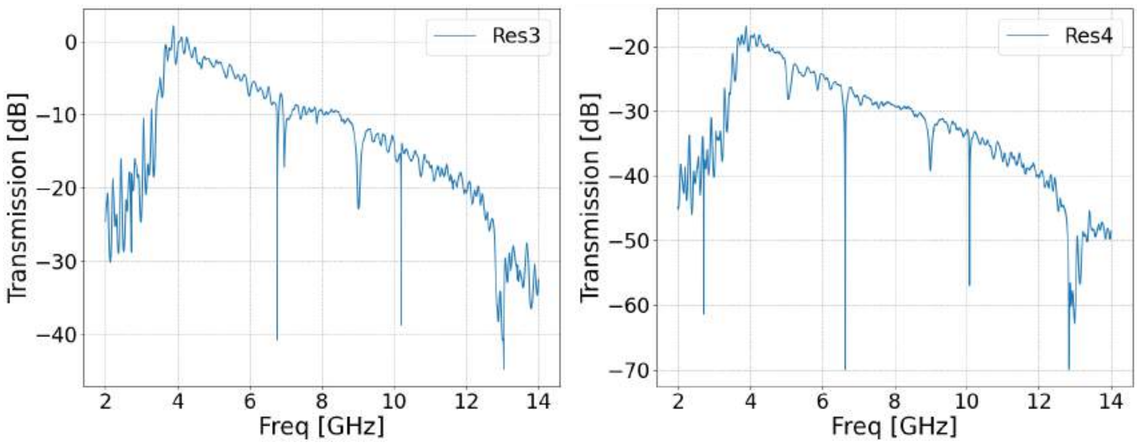

Figure 8.2: Transmission of Res3 and Res4 measured at a VNA power of 0 dBm and -10 dBm with added attenatuion of 0 and 20 dB respectively.

peak of Res3 above 2 GHz is likely due to the increase in VNA power. Also, there is a shift of the transmission, indicating the microwave measurement line had around $\sim$ 10 dB less attenuation. As the measurement time was limited, there was only time to fully measure one of the resonators without top ground. Res4 was therefore chosen. Nevertheless, the data can be used to extract Q-factors, as this quantity does not depend on exact calibration and on features of peaks unrelated to the LC-circuit.

The transmission versus frequency power sweep for the second resonance of Res4 at around 6.6 GHz is shown in Fig. 8.3 for VNA powers between -20 dBm and -9 dBm. As the power goes up, the resonance dip shifts towards lower frequencies. This is explained by the self-Kerr effect [38]. The sinusoidal dependence of the Josephson potential of our nonlinear resonator induces a power dependence of the resonance frequency. The resonance also changes and becomes more and more asymmetric, losing its Lorentzian shape. When going to even higher powers the resonance completely disappears and the transmission makes a jump. For this reason the values have to be discarded at a certain power when fitting the resonances with Eq. 7.1.

Fig. 8.4 shows the transmission for a sweep of the VNA power after adding 40 dB of attenuation. In this power range the resonance frequency does not shift anymore. However the fluctuations become larger so we averaged each VNA trace 15 times. The resonances of Res4 are still quite well pronounced, even when going to the lowest powers we measured in our effective 80 dB range.

The transmission of the top ground (TG) samples is shown in Fig. 8.5. The resonance dips, which correspond to the resonance of our Josephson junction array resonator are more difficult to recognize. But if we look at the transmission at higher power and vary it, we can nicely identify the resonances we are interested in (see Fig. 8.6). The free spectral range is consistent with a calculation done in Appendix A.1. One example resonance at low power is shown in Fig. 8.7. The resonances of the TG samples do not have the same clear shape as the ones from Res4 without TG. Also the fluctuations for the lowest powers become large.

8.2 Extracted quality factors

By fitting Eq. (7.1) to the transmission measurement of the second cooldown for each power value of a resonance, one can obtain a power dependence of the internal quality factor. For the first two measured resonances of TG-Res1, this is shown in Fig. 8.8. As the input power on the

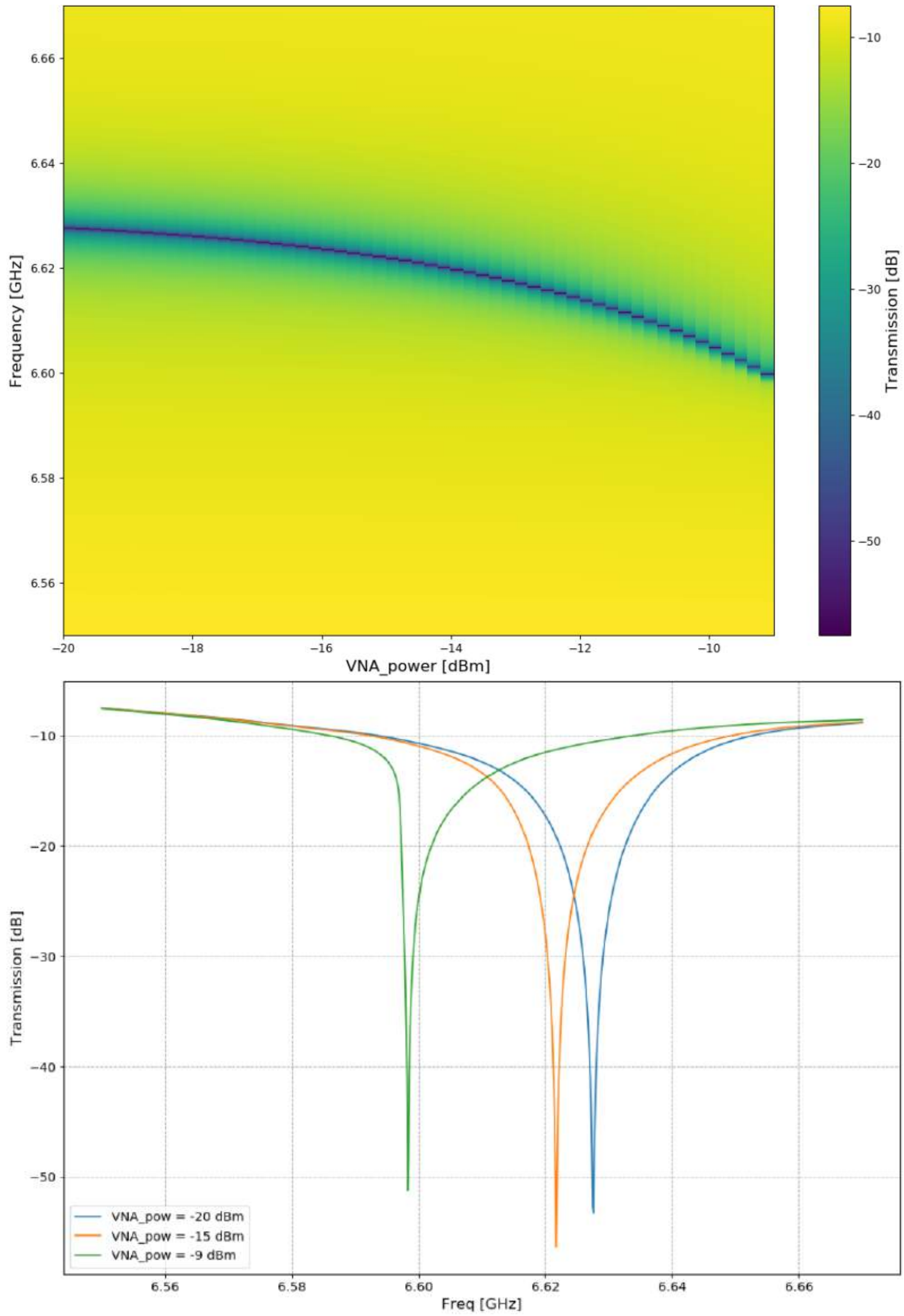

Figure 8.3: Transmission vs frequency for a VNA power sweep. In the high power regime the resonance shifts to lower frequencies when increasing the VNA power.

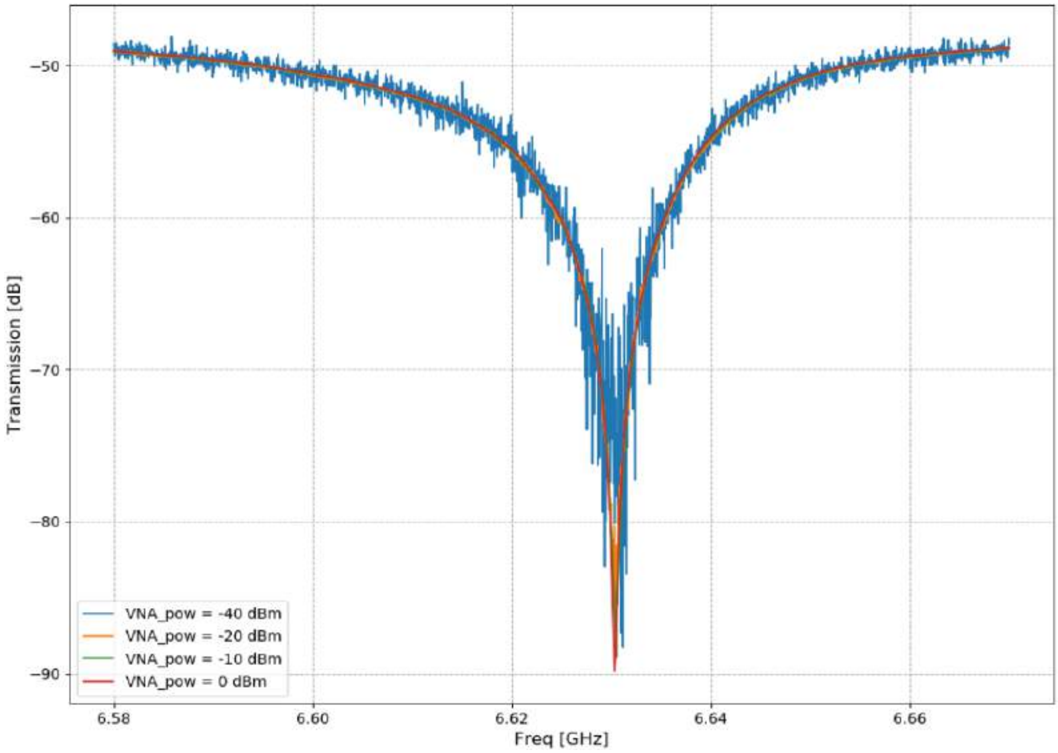

Figure 8.4: Transmission vs frequency for a VNA power sweep at low power with an added 40 dB of attenuation after the VNA output.

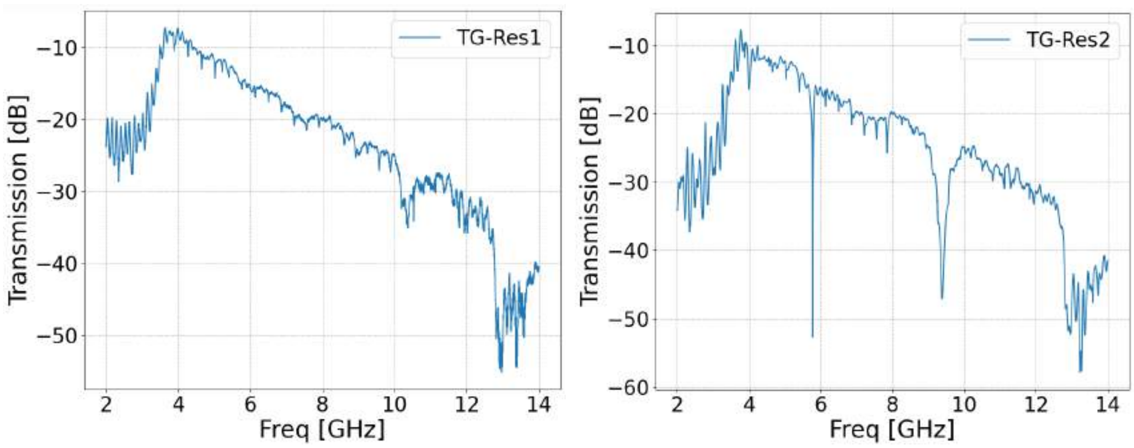

Figure 8.5: Transmission of TG-Res1 and TG-Res2 measured at a VNA power of -10 dBm.

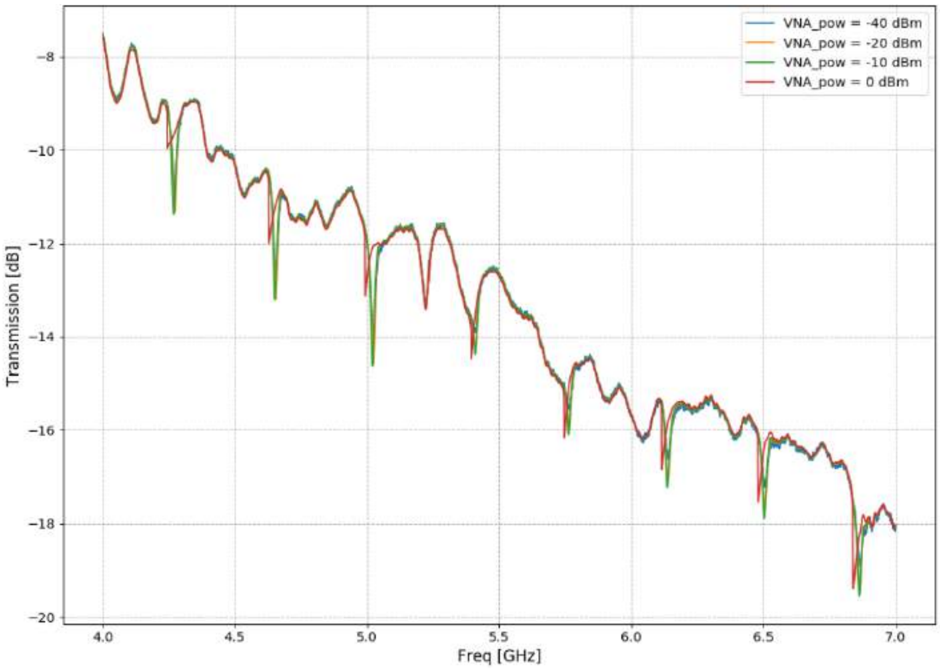

Figure 8.6: Transmission of TG-Res1 at high power in the first frequency range for different VNA powers. By varying the VNA power one can identify the resonances.

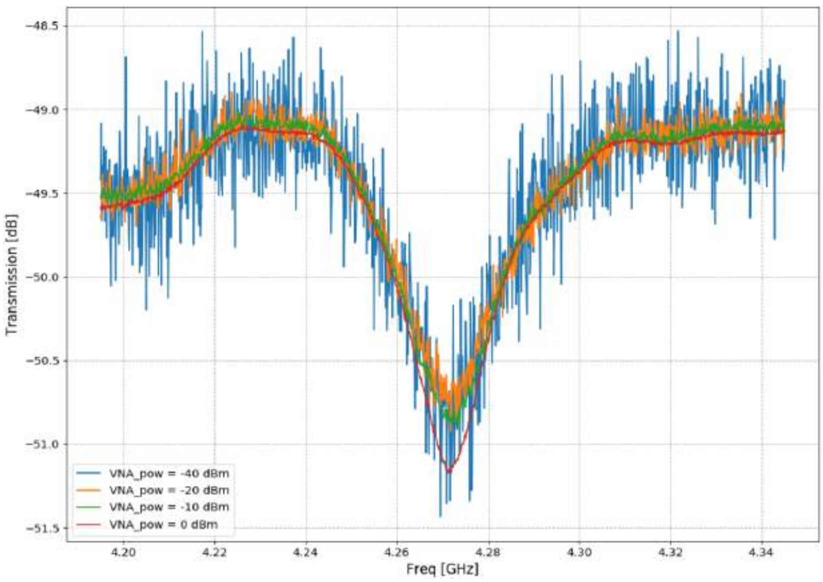

Figure 8.7: Transmission of a resonance of TG-Res1 at low power for four different VNA powers.

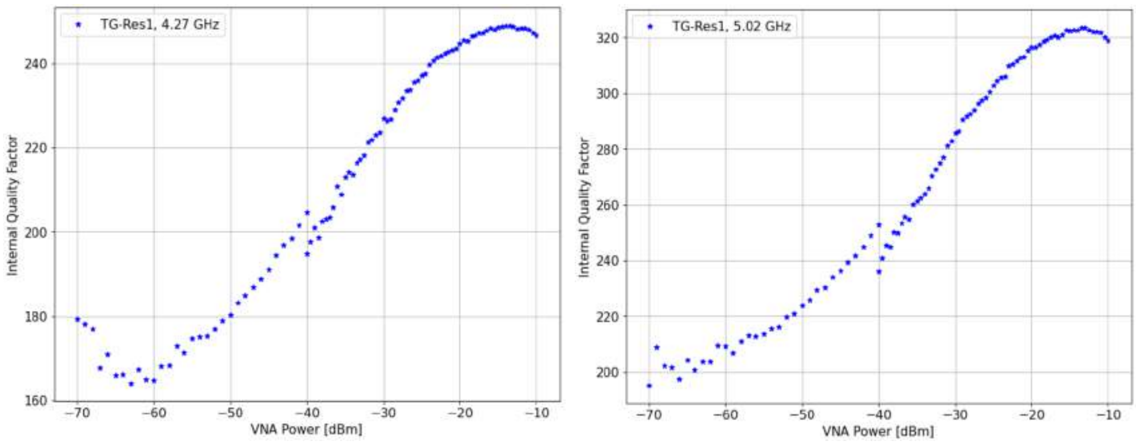

Figure 8.8: Internal quality factors for two measured resonances of TG-Res1 plotted against the VNA power.

resonator is increased, the internal quality factor increases. Since the dielectric loss tangent is inversely proportional to the internal quality factor (Eq. 2.26) the dielectric loss decreases with an increase in power. In the middle of the VNA power range we measured, we see a linear dependence. This behaviour can be explained by the excitation of two-level systems (TLS) at the interface between the superconductor and the dielectric. For high powers we saturate the TLS and the internal quality factor plateaus at some value. On the other hand the Q_i also seem to reach minimal values for very low powers. As we will see by calculation of the average photon number these low power values correspond to the single photon regime. An intrinsic value of the dielectric loss of the material is reached.

The step in the values of Q_i in Fig. 8.8 at -40 dBm VNA power is due to the change in data sets. It is the point where we change from high to low power by adding the 40 dB attenuators and start averaging several times over the traces of each power point. The fits of Q_i to the remaining resonances of TG-Res1 and the resonances of TG-Res2 are listed in the appendix (see. A.4).

When calculating the average number of photons in the resonator by applying Eq. 7.2 with the use of the measured attenuation from the VNA output to the input power of the resonators (see Fig. 5.2), one can estimate for which value of Q_i the average photon number is $\bar{n} \approx 0.1$. For this average number of photons the values of Q_i for all 13 resonances of the two TG samples are plotted in a histogram in Fig. 8.9. We get values of $Q_i = 216 \pm 22$, which corresponds to loss tangents of $\tan(\delta) = (4.7 \pm 0.5) \times 10^{-3}$. These values are in agreement with previous measurements of TG resonators done in [38]. The values obtained for the loss are about ~ 2.5 times higher compared to previous measurements in thin aluminum oxide layers [63].

When performing the fits for the resonances of Res4, much higher quality factors are obtained than for TG-Res1&2. This was expected, considering the much deeper and very thin resonance dips. The results of the fits for the three resonances are shown in Fig. 8.10. The shapes obtained do not show the saturating effects as clearly as the other resonances did. In the considered power ranges, the internal quality factors seem to almost saturate for the resonances at 2.71 GHz and at 10.07 GHz at low power. Especially the plot of the first resonance shows a lot of outliers towards very high quality factors. Here, the automatized fits do not seem to work perfectly for the whole range of power values. A saturation for high VNA powers is not directly observed. Some high power values had to be discarded, because they could not be fitted with the Lorentzian function. The combined results of the internal quality factors are shown in Fig. 8.11. As it is clear from this plot with logarithmic scale, the Q_i for the

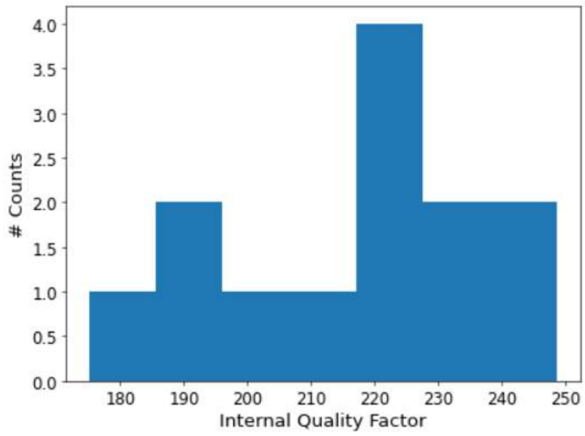

Figure 8.9: Histogram of the Q_i for the TG samples.

resonator without the close ground on top of the resonator array are much higher. The losses in this case are therefore much lower. We conclude that the top ground on the resonator is the cause of the much higher losses.

The values of the quality factors obtained from the fits for the resonances of the different samples is given in table 8.1.

For the external quality factors Q_e we extract values for each resonance as well. As we are using the fits which favour constant Q_e, the obtained values are almost constant with respect to the VNA power. The results are shown in Fig. 8.12. With some outliers, the Q_e for TG-Res1 and TG-Res2 are around ~ 1000. For Res4 the estimated Q_e are in the low hundreds. It is difficult to read off a dependence of Q_e with respect to frequency.

Since Q_e increases when the impedance of the resonator array is lowered, this difference between the samples is expected. The purpose of the close ground on top of the resonator array is to impedance match it to $50\,\Omega$. Without it, the capacitance of the Josephson junctions to ground is much lower and therefore the impedance much higher in the case of Res4, hence a lower Q_e.

From the direct comparison between the two geometries with the only difference being the top ground we can conclude that this top ground is the cause for the increase in losses. The devices without the top ground above the resonator array built in this work can be used as a reference when exploring new geometries and dielectrics. This can help to improve the losses in the future.

Other dielectrics can be experimented with. Amorphous silicon (a-Si) for example shows very promising loss[40]. Also silicon nitride (SiN) or hexagonal boron nitride (h-BN) could be good options to explore[64]. A-Si has been tried before in a similar resonator design and has not led to the expected improvement in the loss. There might be factors in the fabrication process used, which limit the dielectric quality [38]. For the fabrication of the resonators in this work there were steps in the process which were not performed in a cleanroom environment. The DC tests, which are done before deposition of the dielectric, are thought to be one of the major factors leading to a decrease in the dielectric quality together with the water used for the ALD. Coating the wafer with a protective resist before the DC tests, which could be removed again afterwards, might improve the dielectric quality.

Copper, which we used as the top ground of the resonators has an anomalous skin depth. Since gold has also been used before [38] one might want to explore new possibilities. Replacing the top ground out of copper or gold with aluminum could allow to isolate the effect of conductor losses.

Sample	Resonance [GHz]	Q_i	Q_e	P_s [dBm]	$\tan(\delta)$
TG-Res1	4.27	175	736	-129	5.7×10^{-3}
TG-Res1	5.02	220	754	-129	4.5×10^{-3}
TG-Res1	5.76	199	1834	-124	5.0×10^{-3}
TG-Res1	6.50	219	1274	-125	4.6×10^{-3}
TG-Res1	6.86	246	1211	-125	4.1×10^{-3}
TG-Res1	7.22	235	1204	-124	4.3×10^{-3}
TG-Res1	7.90	211	1081	-124	4.7×10^{-3}
TG-Res1	8.60	193	777	-123	5.2×10^{-3}
TG-Res2	3.89	227	1020	-130	4.4×10^{-3}
TG-Res2	5.40	186	803	-127	5.4×10^{-3}
TG-Res2	6.14	230	992	-127	4.3×10^{-3}
TG-Res2	6.50	249	1184	-126	4.0×10^{-3}
TG-Res2	6.90	221	960	-125	4.5×10^{-3}
Res4	2.71	4081	159	-140	2.5×10^{-4}
Res4	6.63	12305	187	-133	8.1×10^{-5}
Res4	10.07	7072	404	-132	1.4×10^{-4}

Table 8.1: Results for the Q-factors of the different fitted resonances. The input power at the resonator for an average photon number of $\bar{n} \approx 0.1$ is estimated as P_s using (7.2). The Q_i listed correspond to these input powers.

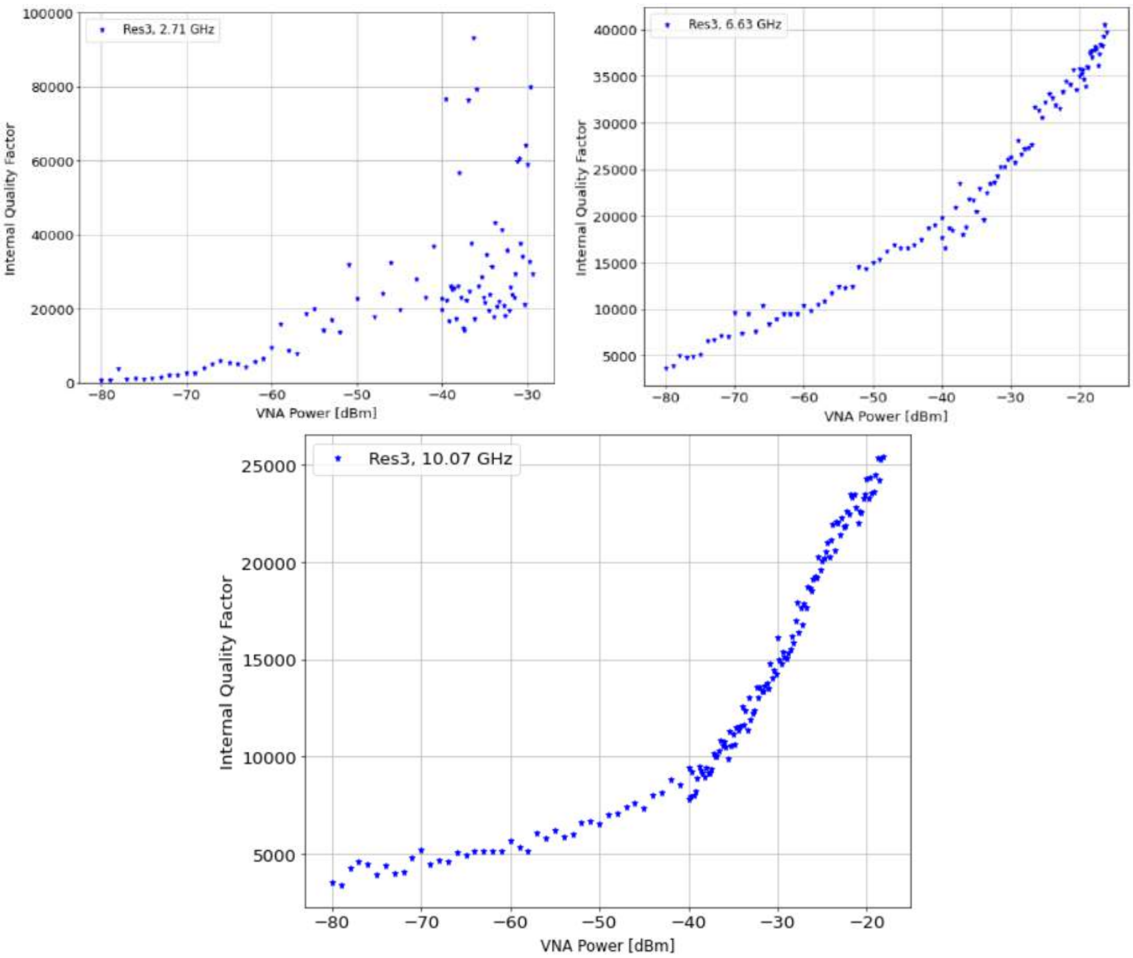

Figure 8.10: Internal quality factors for the resonances of Res4.

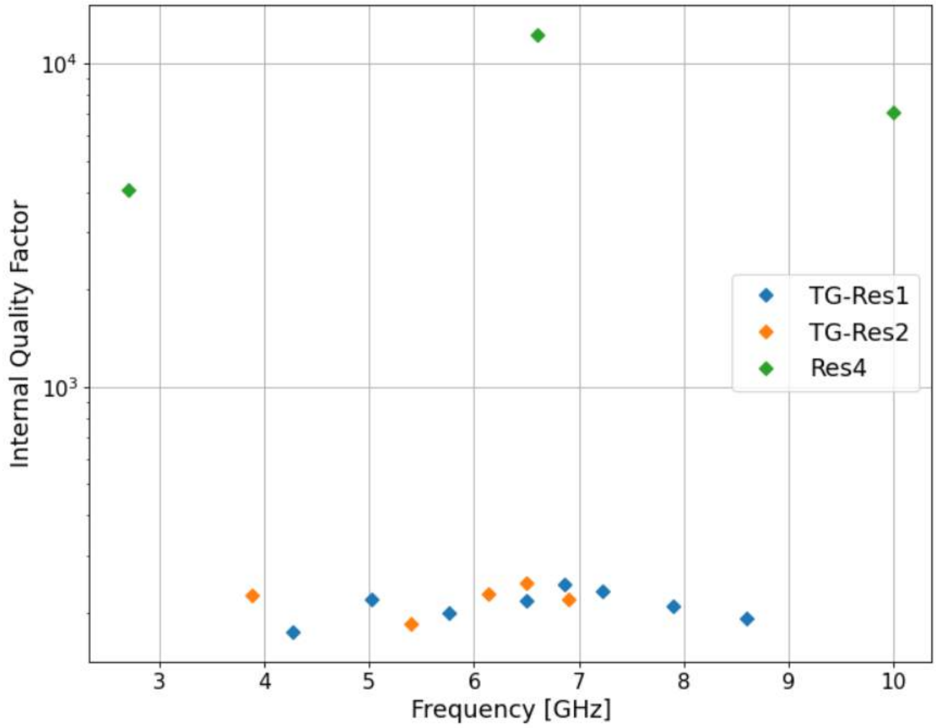

Figure 8.11: Low power Q_i for all measured resonances.

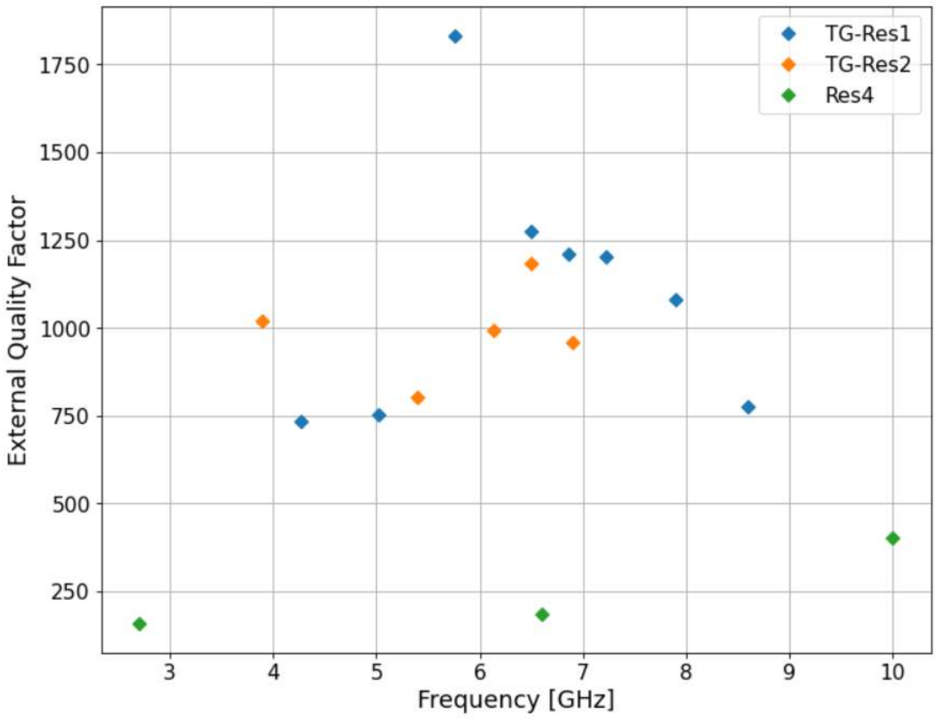

Figure 8.12: Fitted Q_e for all measured resonances.

Chapter 9

Conclusion

We have built and compared two geometries of Josephson junction array based $\lambda/2$ resonators. The effect of a close top ground on the resonator array, which can be used in TWPA to impedance match the Josephson transmission line, leads to measured loss tangents of $\tan(\delta) = (4.7 \pm 0.5) \times 10^{-3}$. The loss tangents are obtained by extracting the quality factors from a fit to the resonances. When leaving out the ground right on top of the resonator array, values of $\tan(\delta) \sim 10^{-4}$ were measured. This shows that the top ground leads to higher losses.

To improve the sensitivity for axion detection at MADMAX, amplifiers reaching near quantum limited noise operating at frequencies above 10 GHz are needed. From results of TWPA operation up to $\sim$ 12 GHz [4] it has become clear that the main hurdle that has to be overcome to develop TWPA working at higher frequencies is their losses.

From measuring the effect of the top ground layer in this work it was demonstrated that the top ground, as it is used for the impedance matching in the TWPA at the moment, leads to an increase in $\tan(\delta)$ which restricts their operation above 10 GHz.

To tackle these challenges, the next steps that should be pursued include the investigation of different dielectrics.

The aluminum based Josephson junctions, which are made with the fabrication process used in this work, have a self resonant frequency of $\sim$ 20 GHz. If losses are minimized so far as to make it possible to operate TWPA at this frequency, another change could be necessary. Other superconductors as components of the Josephson junctions have to be tested, possibly requiring the development of new fabrication methods.

Developing quantum limited amplifiers for the use at MADMAX can pave the way to detect dark matter axions.

Bibliography

[1] MADMAX Working Group collaboration, A. Caldwell, G. Dvali, B. Majorovits, A. Millar, G. Raffelt, J. Redondo, et al. Dielectric haloscopes: A new way to detect axion dark matter. *Phys. Rev. Lett*, 2017.

[2] B. Yurke, L. R. Corruccini, P. G. Kaminsky, L. W. Rupp, A. D. Smith, A. H. Silver, R. W. Simon, and E. A. Whittaker. Observation of parametric amplification and deamplification in a josephson parametric amplifier. *Phys. Rev. A*, 1989.

[3] C. Macklin, K. O'Brien, D. Hover, M. Schwartz, V. Bolkhovsky, X. Zhang, W. Oliver, and I. Siddiqi. A near–quantum-limited josephson traveling-wave parametric amplifier. *Science*, 2015.

[4] Martina Esposito, Arpit Ranadive, Luca Planat, Nicolas Roch, et al. Perspective on traveling wave microwave parametric amplifiers. *Appl. Phys. Lett. 119*, 2021. arXiv:2107.13033v5.

[5] F. Zwicky. Die Rotverschiebung von extragalaktischen Nebeln. *Helv. Phys. Acta*, 1933.

[6] Virginia Trimble. Existence and nature of dark matter in the universe. *Annual Review of Astronomy and Astrophysics, 25(1)*, 1987.

[7] G. Bertone, D. Hooper, and J. Silk. Particle dark matter: Evidence, candidates and constraints. *Phys. Rev. Lett.*, 1978.

[8] M. Pospelov and A. Ritz. Theta vacua, qcd sum rules, and the neutron electric dipole moment. *Nucl. Phys. B 573*, 2000.

[9] J. M. Pendlebury et al. Revised experimental upper limit on the electric dipole moment of the neutron. *Phys. Rev. D92*, 2015.

[10] R. D. Peccei and H. R. Quinn. Cp conservation in the presence of instantons. *Phys. Rev. Lett.*, 1977.

[11] R. D. Peccei and H. R. Quinn. Constraints imposed by cp conservation in the presence of instantons. *Phys. Rev. Lett.*, 1977.

[12] G. Grilli di Cortona, E. Hardy, J. Pardo Vega, and G. Villadoro. The qcd axion, precisely. 2010. https://arxiv.org/abs/1511.02867.

[13] A. Millar, J. Redondo, and F. Steffen. Dielectric haloscopes: sensitivity to the axion dark matter velocity. 2018. arXiv:1707.04266v3.

[14] Stefan Knirck. How to search for axion dark matter with madmax (magnetized disk and mirror axion experiment), 2020.

[15] D. Horns, J. Jaeckel, A. Lindner, et al. Searching for wispy cold dark matter with a dish antenna. *JCAP*, 2013.

[16] S. Borsanyi et al. Calculation of the axion mass based on high-temperature lattice quantum chromodynamics. *Nature volume 539*, 2016.

[17] The MADMAX collaboration, A. Caldwell P. Brun, L. Chevalier, et al. A new experimental approach to probe qcd axion dark matter in the mass range above 40ev. *The European Physical Journal C*, 2019.

[18] T. Hiramatsu et al. Production of dark matter axions from collapse of string-wall systems. *Phys. Rev. D 85*, 2012.

[19] M. Kawasaki, K. Saikawa, and T. Sekiguchi. Axion dark matter from topological defects. *Phys. Rev. D 91*, 2015.

[20] P. Sikivie. Experimental tests of the invisible axion. *Phys. Rev. Lett*, 1983.

[21] S. Asztalos et al. Improved rf cavity search for halo axions. *Phys. Rev. D 69*, 2004.

[22] B. Brubaker, L. Zhong, Y. Gurevich, et al. First results from a microwave cavity axion search at 24 micro-ev. *Phys. Rev. Lett. 118*, 2017.

[23] L. Zhong, S. Kenany, K. Backes, et al. Results from phase 1 of the haystac microwave cavity axion experiment. *Phys. Rev. D 97*, 2018.

[24] D. Budker et al. Cosmic axion spin precession experiment (casper). *Phys. Rev. X 4*, 2014.

[25] J. Ouellet et al. First results from abracadabra-10 cm: A search for sub-ev axion dark matter. *Phys. Rev. Lett. 122*, 2019.

[26] MADMAX collaboration, S. Beurthey, N. Böhmer, P. Brun, A. Caldwell, L. Chevalier, C. Diaconu, et al. Madmax status report. 2020.

[27] A. Millar, G. Raffelt, J. Redondo, and F. Steffen. Dielectric haloscopes to search for axion dark matter: Theoretical foundations. *JCAP 1701:061*, 2017.

[28] T. Hunter and R. Kimberk. Statistical topics concerning radiometer theory. 2015. arXiv:1507.04280.

[29] J. Kraus. *Antennas and wave propagation.* Mc Graw Hill, isbn:0070671559 edition, 2010.

[30] C. Caves. Quantum limits on noise in linear amplifiers. *Phys. Rev. D.*, 1981.

[31] A. Clerk, M. Devoret, S. Girvin, F. Marquardt, and R. Schoelkopf. Introduction to quantum noise, measurement, and amplification. *Rev. Mod. Phys. 82*, 2010.

[32] Takashi Mimura et al. Enhancement-mode high electron mobility transistors for logic applications. *Jpn. J. Appl. Phys. 20*, 1982.

[33] Low Noise Factory. Datasheet 4-8 GHz Cryogenic Low Noise Amplifier. `https://quantummicrowave.com/wp-content/uploads/2023/01/lnf-lnc4_8sf.pdf`. 2023.

[34] Caterina Braggio, Giulio Cappelli, Giovanni Carugno, Nicolò Crescini, Raffaele Di Vora, Martina Esposito, Antonello Ortolan, Luca Planat, Arpit Ranadive, Nicolas Roch, and Giuseppe Ruoso. An haloscope amplification chain based on a travelling wave parametric amplifier. 2022. arXiv:2205.02053.

[35] K. C. Gupta, Ramesh Garg, and Inder J. Bahl. Microstrip lines and slotlines. 1979.

[36] Luca Planat, Ekaterinna Al-Tavil, Javier Puertas Martínez, Rémy Dassonneville, et al. Fabrication and characterization of aluminum squid transmission lines. *Phys. Rev. Applied 12*, 2019.

[37] David M. Pozar. *Microwave Engeneering*. 4th edition edition.

[38] Luca Planat. Resonant and traveling-wave parametric amplification near the quantum limit, 2020.

[39] M. Von Schickfus and S. Hunklinger. Saturation of the dielectric absorption of vitreous silica at low temperatures. *Physics Letters A*, 1977.

[40] Aaron D. O'Connell, M. Ansmann, and R. C. Bialczak. Microwave dielectric loss at single photon energies and millikelvin temperatures. *Physics letters*, 2008.

[41] J. Martinis, K. Cooper, R. McDermott, et al. Decoherence in josephson qubits from dielectric loss. *Phys. Rev. Lett. 95*, 2005.

[42] Werner Buckel and Reinhold Kleiner. *Supraleitung*. Wiley-VCH.

[43] Brian D. Josephson. Possible new effects in superconductive tunnelling. *Physics letters*, 1962.

[44] Julien Claudon. Coherent oscillations in a quantum superconducting circuit : the dc squid, 2005.

[45] M. H. Devoret, A. Wallraff, and J. M. Martinis. Superconducting qubits: A short review.

[46] P. D. Nation, J. R. Johansson, M. P. Blencowe, and Franco Nori. Stimulating uncertainty: Amplifying the quantum vacuum with superconducting circuits. *Rev. Mod. Phys. 84*, 2012.

[47] Benjamin M. Brubaker. First results from the haystac axion search, 2018. arXiv:1801.00835.

[48] Samuel Boutin, David M. Toyli, Aditya V. Venkatramani, et al. Effect of higher-order nonlinearities on amplification and squeezing in josephson parametric amplifiers. *Phys. Rev. Applied 8*, 2017.

[49] J. Bourassa, F. Beaudoin, Jay M. Gambetta, and A. Blais. Josephson-junction-embedded transmission-line resonators: From kerr medium to in-line transmon. *Phys. Rev. A 86*, 2012.

[50] Arpit Ranadive, Martina Esposito, Luca Planat, et al. Kerr reversal in josephson metamaterial and traveling wave parametric amplification. *Nat. Comm. 13, 1737*, 2022.

[51] Etienne Dumur. A v-shape superconducting artificial atom for circuit quantum electrodynamics, 2015.

[52] K.J. BINNS and P.J. LAWRENSON. *Analysis and computation of electric and magnetic field problems*. Pergamon Press, 1973.

[53] Javier Puertas-Martinez. Probing light-matter interaction in the many- body regime of superconducting quantum circuits, 2018.

[54] G. J. Dolan. Offset masks for lift-off photoprocessing. *Appl. Phys. Lett. 31, 337*, 1977.

[55] V. Ambegaokar and A. Baratoff. Tunneling between superconductors. *Phys. Rev. Lett. 10, 486*, 1963.

[56] John F. Cochran and D. E. Mapother. Superconducting transition in aluminum. *Phys. Rev. Lett. 111, 1*, 1958.

[57] Rémy Dassonneville. Qubit readouts using a transmon molecule in a 3d circuit quantum electrodynamics architecture, 2019. https://theses.hal.science/tel-02274266.

[58] N. H. Balshaw. Practical Cryogenics. `http://research.physics.illinois.edu/bezryadin/links/practical%20cryogenics.pdf`. 2001.

[59] Frank Pobell. *Matter and Methods at Low Temperatures.* Springer, isbn: 978-3-540-46360-3 edition, 2007.

[60] User:Sakurambo, Wikimedia. Loss tangent phasors 1.svg. `https://upload.wikimedia.org/wikipedia/commons/6/61/Loss_tangent_phasors_1.svg`. 2009.

[61] Rui Igreja and C.J. Dias. Analytical evaluation of the interdigital electrodes capacitance for a multi-layered structure. *Elsevier*, 2004.

[62] Sonnet Software, Inc. Sonnet Software. `https://www.sonnetsoftware.com/about/`. 2023.

[63] Chunqing Deng, M. Otto, and A. Lupascu. Characterization of low-temperature microwave loss of thin aluminum oxide formed by plasma oxidation. *Phys. Rev. Applied*, 2014.

[64] Julia Zotova, Rui Wang, Alexander Semenov, et al. Compact superconducting microwave resonators based on Al/AlOx/Al capacitor. 2022. arXiv:2203.09592.

List of Figures

Appendix A

Appendix

A.1 Calculation of Free Spectral Range for Resonators With Top-Ground

To estimate the free spectral range we take the values obtained during the DC-tests (Sec. 4.2.3). With (Eq. 4.1) we obtain the value $I_c = 2.25\,\mu\text{A}$ for the critical current of the junctions. The Josephson inductance is then $L_J = 146.12\,\text{pH}$. To account for a later change in the Josephson junctions after the heating during the ALD process and the cooling in the cryostat later, which changes their inductance, we set $L_{J,20\text{mK}} = \alpha_B\,\alpha_{\text{ALD}}\,L_J = 161.46\,\text{pH}$ with factors $\alpha_B = 1.3$ and $\alpha_{\text{ALD}} = 0.85$.

As we chose $N_c = 220$ as the number of cycles for the ALD process, we assume a thickness of the alumina layer of about $t_d \approx 22\,\text{nm}$. The capacitance to ground by one unit cell of the junction array with junction area $A_J = (10.5\times0.8)\mu\text{m}^2$ and wire area $A_W = (0.35\times2.447)\mu\text{m}^2$ is then given by $C_g = \epsilon_0\epsilon_{\text{AlOx}}A_{\text{sum}}/t = 36.5\,\text{fF}$ with $A_{\text{sum}} = 9.26\,\mu\text{m}^2$ and $\epsilon_{\text{AlOx}} = 9.8$. The impedance of the array is then given by

$$Z_0 = \sqrt{\frac{L_{J,20\text{mK}}}{C_g}} = 66.51\,\Omega\,. \tag{A.1}$$

By applying the boundary condition for a $\lambda/2$ resonator (Eq. 3.28) we get the free spectral range

$$\Delta f = \frac{v_\phi}{\lambda_1} = \frac{v_\phi}{2\ell} \approx 335\,\text{MHz} \tag{A.2}$$

with the length $\ell \approx 2\,\text{mm}$ and the phase velocity

$$v_\phi = \frac{a}{\sqrt{L_{J,20\text{mK}}C_g}} \approx 1.34\times10^6\text{m/s}\,. \tag{A.3}$$

A.2 Estimation of Feedline Impedance with TXLINE

To check, if the assumption for the feedline impedance of $Z_0 = 50\,\Omega$ is justified, we estimate it with the program *TXLINE*. To simulate superconducting aluminum, we set its conductivity to $\sigma > 10^{15}$. We have a feedline width of $W = 238\,\mu\text{m}$, a gap to the copper top ground of $240\,\mu\text{m}$, a height of the feedline of $70\,\text{nm}$ and a distance to the ground on the bottom of the wafer of 275 µm. If we now us silicon with a dielectric constant of $\epsilon_r = 11.9$ as the substrate, we get an impedance of 45.64 Ω (see Fig. A.1). This is off by a few Ohm.

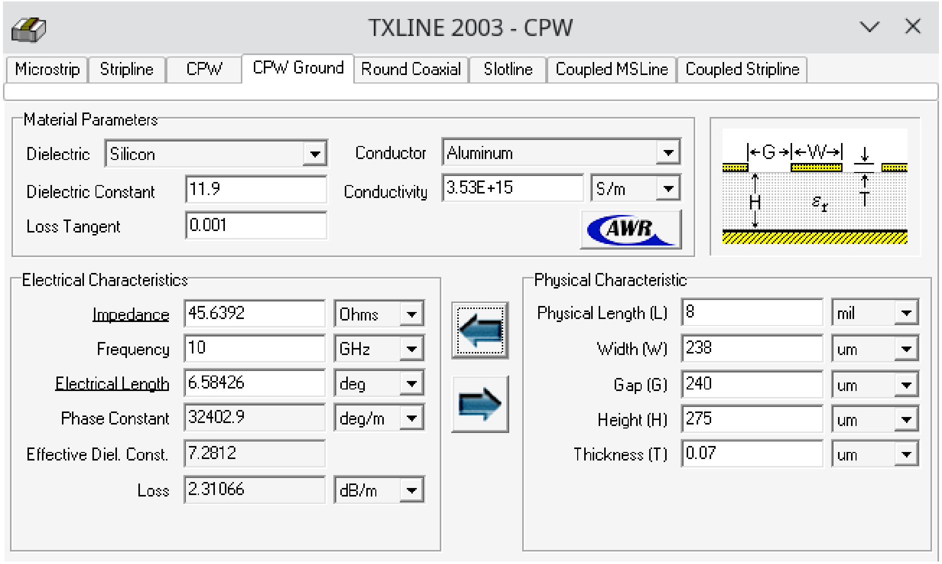

Figure A.1: Simulation with silicon substrate.

When using alumina as a substrate (which seems unjustified, since it is only deposited as a very thin layer on top of the feedline), we arrive at an impedance close to 50 Ω (see Fig. A.2

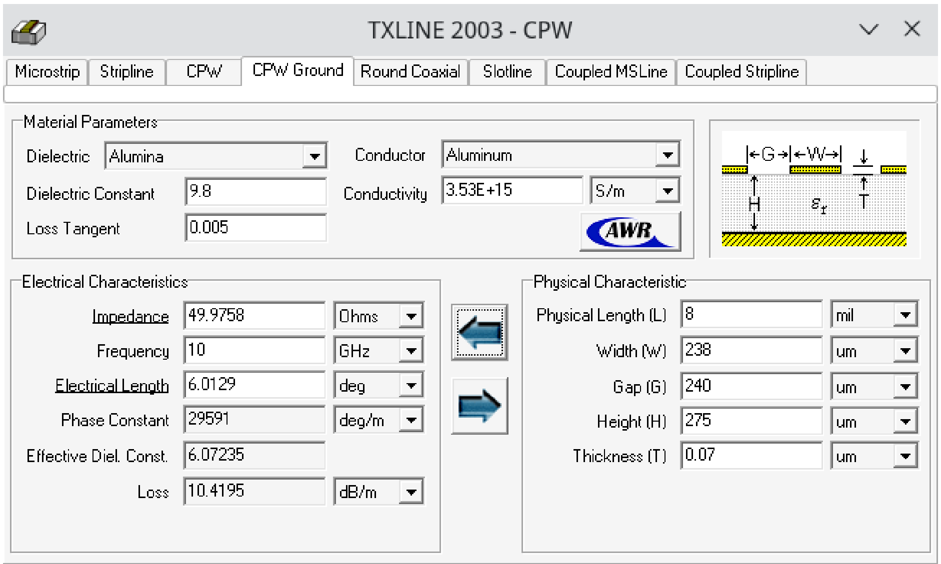

Figure A.2: Simulation with alumina substrate.

Modeling the feedline as a CPW without ground, the values are found to be in the 60-70 Ω range and even higher for different substrates.

A.3 Comparison of the VNAs

During the first cooldown the transmissions were measured using the ZNL14 VNA and the MS46522B VNA. For the measurements with low power the ZNL14 seemed to perform just slightly better. The transmission for Res3 and Res4 are shown in Fig. A.3. They are practically the same as what we measured with the ZNL14 (see. 8.1). Since the ZNL14 can

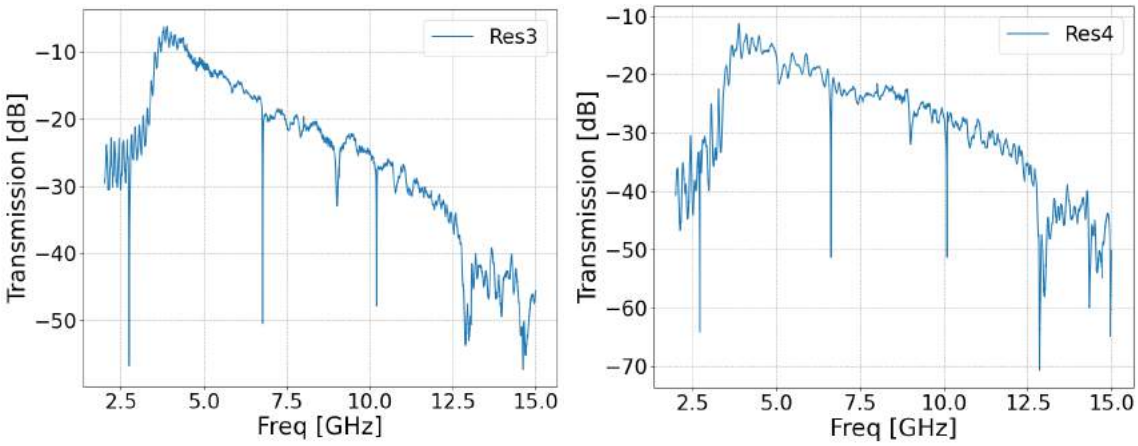

Figure A.3: The transmission $|S_{21}|$ of Res3 and Res4 measured with the Anritsu VNA at a power of -10 dBm.

sweep 40 dB of power without changing attenuators on the output (compared to 30 dB for the MS46522B) and just arrived new a few days before, we decided to use it for all further measurements.

A.4 Plots of Q_i vs Power for Remaining Resonances

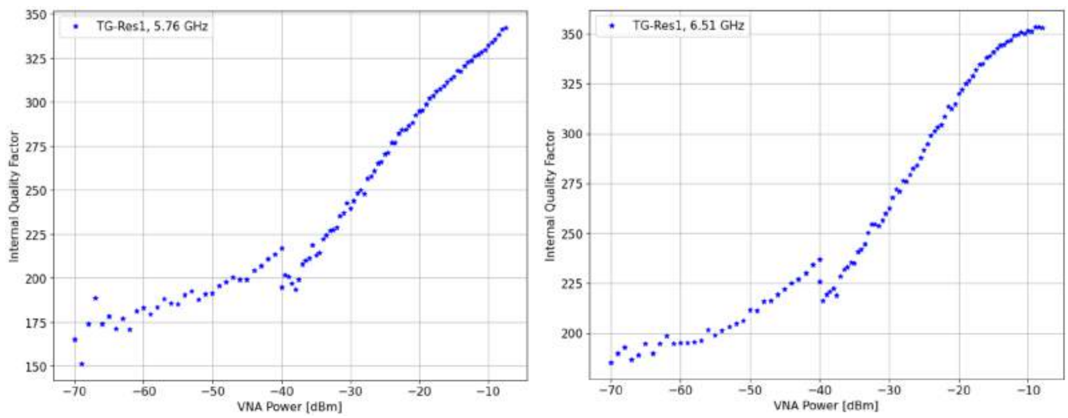

Figure A.4: Internal quality factors versus VNA power for the remaining resonances of TG-Res1. (a)

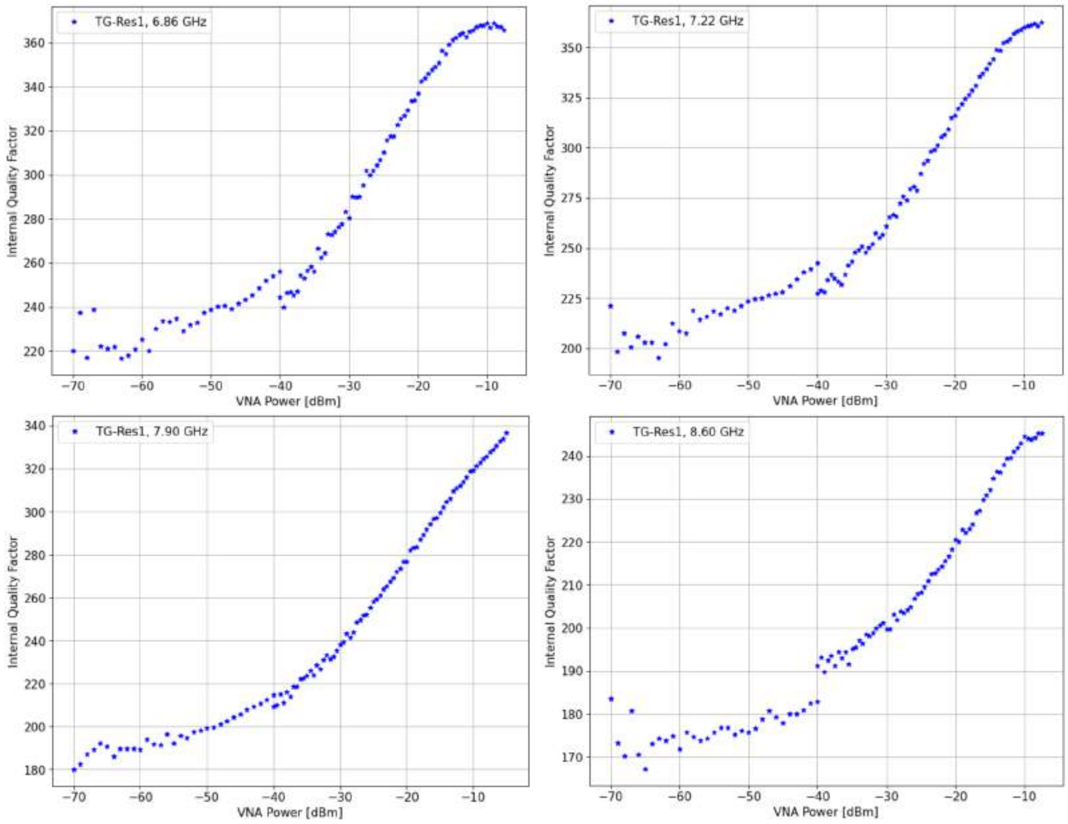

Figure A.5: Internal quality factors versus VNA power for the remaining resonances of TG-Res1. (b)

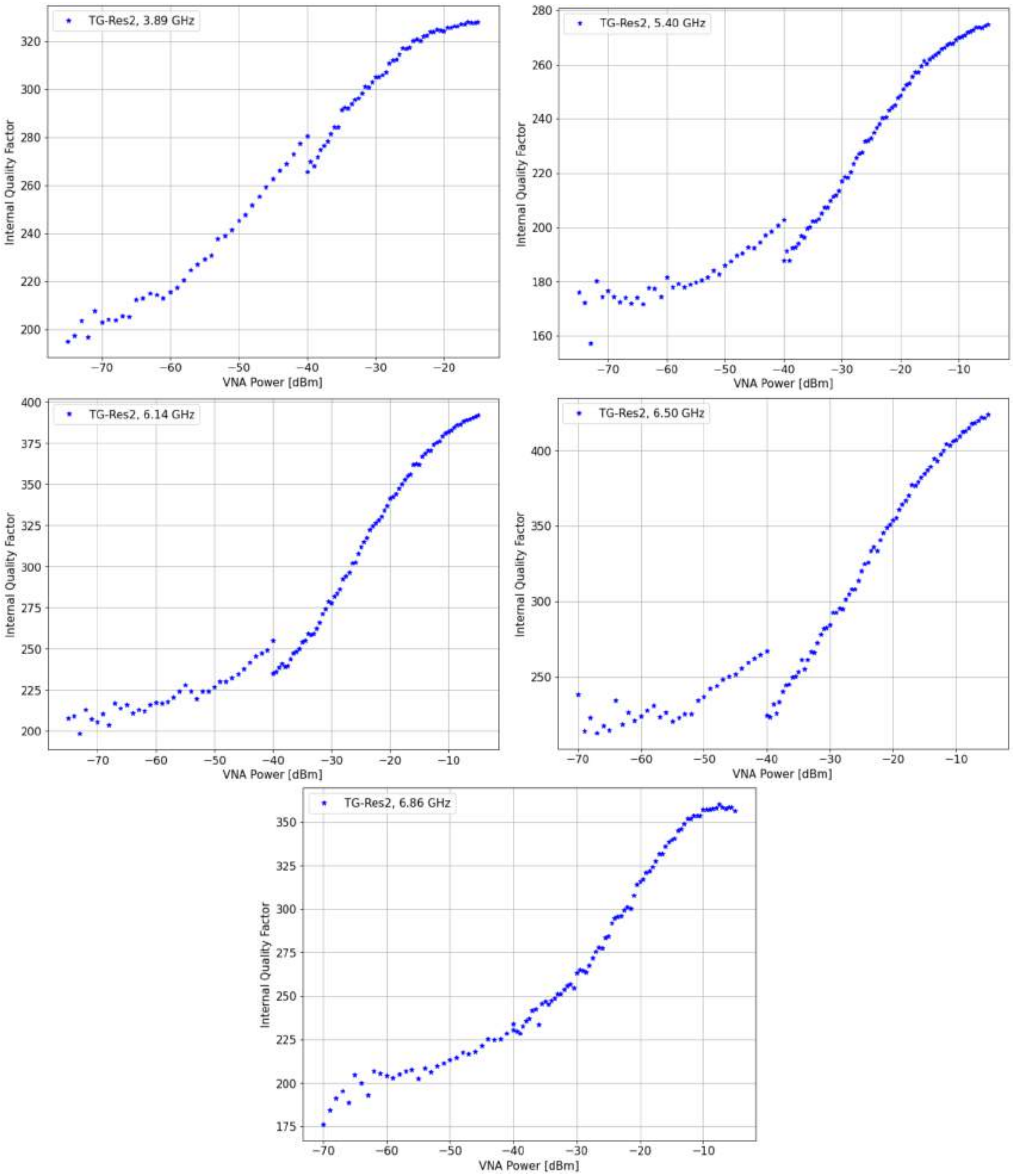

Figure A.6: Internal quality factors versus VNA power for the fitted resonances of TG-Res2.

Selbständigkeitserklärung

Ich versichere hiermit, die vorliegende Arbeit mit dem Titel

Towards Quantum Limited Detectors for the MADMAX Axion Dark Matter Search: Investigation of Dielectric Losses in Josephson Parametric Amplifiers

selbständig verfasst zu haben und keine anderen als die angegebenen Quellen und Hilfsmittel verwendet zu haben.

Vorname Name

München, den 15. März 2023